nature communications

Article

https://doi.org/10.1038/s41467-024-55038-8

Integrated multi-omics profiling reveals neutrophil extracellular traps potentiate Aortic dissection progression

Received: 4 December 2023

Accepted: 27 November 2024

Published online: 30 December 2024

Check for updates

Yu-Fei Zhao[1,2,3,4,8], Zi-Ang Zuo[1,2,3,8], Zhe-Yun Li[1,2,3], Ye Yuan[1,2,3], Shi-Chai Hong[5,6], Wei-Guo Fu[1,2,3,5,6], Bin Zhou[7] & Li-Xin Wang[1,2,3,5,6]

Adverse aortic remodeling increases the risk of aorta-related adverse events (AAEs) after thoracic endovascular aortic repair (TEVAR) and affects the overall prognosis of aortic dissection (AD). It is imperative to delve into the exploration of prognostic indicators to streamline the identification of individuals at elevated risk for postoperative AAEs, and therapeutic targets to optimize the efficacy of TEVAR for patients with AD. Here, we perform proteomic and single-cell transcriptomic analyses of peripheral blood and aortic lesions, respectively, from patients with AD and healthy subjects. The integrated multi-omics profiling identifies that highly phenotype-associated macrophages orchestrate neutrophil extracellular traps (NETs) through CXCL3/CXCR2 axis, thereby promoting the development of AD. Increased NETs formation is a defining feature of systemic immunity and aortic microenvironment of AD. Inhibiting NETs formation through the blockade of citrullinated histone H3 or CXCL3/CXCR2 axis ameliorates the progression and rupture of aortic dissection in male mice. The plasma level of citrullinated histone H3 predicts AAEs following endovascular therapy, facilitating the risk stratification and prognostic evaluation for patients with AD.

Over the past few decades, significant progress has been made in the treatment of aortic dissection (AD), a life-threatening condition caused by a tear in the intimal layer of the aorta that allows blood to surge into the wall of the tissue, leading to the formation of true and false lumens. Minimally invasive thoracic endovascular aortic repair (TEVAR) has proven effective in stabilizing the dissected aorta with benefit for patients in the early stages of AD[1,2]. However, TEVAR adeptly seals the proximal tear and leaves distal entries open, resulting in an imbalanced blood flow distribution to the distal aorta. In certain patients, persistent blood flow from the true lumen into the false lumen via distal entries contributes to suboptimal or adverse aortic remodeling, thereby increases the risk of aorta-related adverse events (AAEs), and subsequently diminishes overall prognosis of AD[3–6]. Thus, predicting the risk factors for future AAEs in patients with AD is crucial to determine a therapeutic strategy. A comprehensive understanding of the onset and progression of AD is necessary to facilitate the exploration of risk factors that can predict the prognosis of patients with AD and identify those at high risk of postoperative AAEs, ultimately optimizing the efficacy of TEVAR.

[1]Department of Vascular Surgery, Zhongshan Hospital, Fudan University, 200032 Shanghai, China. [2]Vascular Surgery Institute of Fudan University, Fudan University, 200032 Shanghai, China. [3]National Clinical Research Center for Interventional Medicine, Zhongshan Hospital, Fudan University, 200032 Shanghai, China. [4]Department of Liver Surgery and Transplantation, Liver Cancer Institute, Zhongshan Hospital, Fudan University and Key Laboratory of Carcinogenesis and Cancer Invasion, Ministry of Education, 200032 Shanghai, China. [5]Department of Vascular Surgery (Xiamen), Zhongshan hospital, Fudan University, 361015 Xiamen, China. [6]Xiamen Municipal Vascular Disease Precise Diagnose & Treatment Lab, Xiamen, China. [7]State Key Laboratory of Cell Biology, Shanghai Institute of Biochemistry and Cell Biology, Center for Excellence in Molecular Cell Science, Chinese Academy of Sciences, University of Chinese Academy of Sciences, 200031 Shanghai, China. [8]These authors contributed equally: Yu-Fei Zhao, Zi-Ang Zuo. e-mail: wang.lixin@zs-hospital.sh.cn

To monitor the aortic remodeling, recent studies mainly focus on the clinical manifestation and anatomical and morphological changes of aorta based on imaging methods. Several clinical and imaging-related risk factors have been shown to be associated with early disease progression[7–12]. Established risk factors such as the thrombus in the false lumen[13] and the angle of aortic arch[14] are closely associated with postoperative aortic remodeling. The evaluation of morphological change of aorta often relies on computed tomography angiography or magnetic resonance angiography, while can be applied only under certain circumstances due to large radiation dose, high cost of examination, contrast agent-induced nephropathy, and failing to provide functional or dynamic assessment. Serum biomarkers could accurately reflect the pathophysiological changes in the process of disease occurrence and development. In recent years, some progress has been made concerning the diagnosis and prognosis of AD, including D-dimer, inflammation and lipid metabolism associated markers, smooth muscle cell and extracellular matrix related markers, microRNA, and cell-free DNA, which may act synergistically with established clinical risk factors to identify individuals at high risk for poor aortic remodeling[15–17]. Due to the limited sensitivity and specificity, inconsistent results between different studies, and the lack of case of subacute and chronic acute dissection, quite a part of the existing candidate biomarkers are still in the preclinical stage.

Single-cell sequencing enables the comprehensive characterization of cells in a complex and heterogeneous tissue ecosystem, which is of indispensable importance to facilitate prognostic biomarker discovery and cell type targeted therapy[18–20]. However, most expression-based assays that are clinically used rely on bulk transcriptional analysis. Bulk RNA sequencing measures the averaged properties of whole tissue from large samples and provides comprehensive clinical and pathologic phenotype information[21,22]. Therefore, leveraging valuable and widely available phenotype information in bulk data to guide cell subpopulation identification from single-cell data is a promising approach to exploring and interpreting single-cell data from a new perspective.

Here, we perform the integrated multi-omics profiling to identify highly phenotype-associated macrophages orchestrate neutrophil extracellular traps (NETs) through CXCL3/CXCR2 axis in fueling the development of AD. Inhibiting NETs formation through the blockade of CitH3 formation or CXCL3/CXCR2 axis could ameliorate the progression and rupture of AD in mice. The plasma level of citrullinated histone H3 predicts aorta-related adverse events following endovascular therapy, and thereby, facilitate the risk stratification and prognostic evaluation for patients with AD.

Results

AD is marked by systemic inflammation and neutrophil activation in peripheral blood

We conducted a proteomic analysis comparing the plasma samples of 30 patients with acute AD and 30 matched healthy individuals, which were screened from a total of 128 subjects, with the data-independent acquisition quantitative proteomic approach using mass spectrometry. The age at onset and gender did not differ between patients with AD and matched controls after an exact matching, indicating a proper matching quality. (Supplementary Table 1). Other baseline characteristics including AD etiologically related history of hypertension, inflammatory indicators, and D-dimer were statistically significant between two groups (Supplementary Table 1). The resulting differential expression protein profile revealed a marked increase in serum amyloid protein (SAA), C-reactive protein (CRP) and other common inflammatory cytokines in the peripheral blood of AD patients (Fig. 1B). Through gene set enrichment analysis (GSEA), we identified the altered hallmark pathways in patients with AD. These pathways include systemic inflammation, immune response, leukocyte chemotaxis, and neutrophil recruitment and migration, which may indicate the dynamic changes and imbalance of peripheral immunity (Fig. 1C and Supplementary Fig. 1A–F). Additionally, gene ontology (GO) enrichment analysis revealed a significant enrichment of pathways related to protein-DNA subunit organization, complex assembly, nucleosome organization, and assembly in the peripheral blood (Fig. 1D). Furthermore, Kyoto Encyclopedia of Genes and Genomes (KEGG) analysis showed a significant enrichment of pathways associated with neutrophil extracellular traps (NETs) formation (NETosis), platelet activation and actin regulation (Fig. 1E).

The above findings revealed evidence of intricate systemic inflammation activation and the occurrence of immune responses in peripheral blood during AD. Consequently, we could extrapolate that the formation of NETs might play a pivotal role in the pathogenesis of AD.

A phenotype-associated macrophage subset orchestrates neutrophil within aortic microenvironment

We next proceeded to investigate the immune microenvironment within aortas from three healthy individuals and three patients with acute AD. Following the exclusion of damaged or dead cells and putative cell doublets, a total of 47,303 qualified cells were obtained for subsequent single-cell RNA-sequencing analysis. Among these, 28,428 cells were derived from healthy aortas, while 18,875 cells originated from diseased aortas. Utilizing an integrative unsupervised cell clustering analysis (refer to Methods section), the cells were then visualized on a two-dimensional Uniform Manifold Approximation and Projection (UMAP) plot (Fig. 2A).

The 20 distinct cell clusters observed in this study encompassed various clusters of cells grouped into myeloid cells, lymphocytes, and stromal cells (Fig. 2A). Each cluster was carefully annotated using its corresponding markers (Supplementary Figs. 2A, 2B, and 3A). Myeloid cells contained five clusters of macrophages, dendritic cells (DCs), and neutrophils. Lymphocytes encompassed two clusters of T lymphocytes, B lymphocytes, as well as two clusters of plasma cells. Stromal cells included endothelial cells (ECs), smooth muscle cells (SMCs), fibroblasts, myofibroblasts, and macrophage-like fibroblasts.

The macrophages observed in the dissected aorta displayed significant heterogeneity, manifesting various phenotypes. Despite their prevalence as the largest cell population within the aorta, the comprehensive clustering analysis revealed overlapping gene expression patterns among different macrophage populations (Supplementary Fig. 2A), making it difficult to definitively identify distinct subsets of macrophages within the aortas. The subsequent Gene Ontology (GO) analysis showed only moderate differences in their functions among the five macrophage populations (Supplementary Fig. 3B-F).

Three distinct macrophage clusters were found to accumulate significantly in dissected aortas. Cluster 1, the most enriched cluster, exhibited particularly high expression levels of FCGR3A, as well as various pro-inflammatory chemokines and cytokines. These findings suggest that the cells in this cluster are pro-inflammatory lesioned macrophages and will henceforth be referred to as inflammatory macrophages or FCGR3A^{+} macrophages. Cluster 5, on the other hand, displayed upregulated genes that are characteristic of myeloid-derived suppressor cells (MDSCs), including S100A8/9/12 and FCN1 (refs. 23,24). As a result, we classify this cluster as MSDCs-like macrophages. Lastly, cluster 3 showed significant enrichment of OLR1 (ref. 25) and PLIN2, which are markers associated with cholesterol metabolism and lipid accumulation. This subset of macrophages resembles the TREM2^{hi} foamy macrophages previously identified in mouse atherosclerosis[26], and thus referred to as OLR1^{+} macrophages. Macrophage cluster 7 predominantly localized in normal aortas and exhibited gene expression patterns consistent with the known tissue-resident macrophages[27,28]. While cluster 13 showed almost exclusive expression of CD3D, CD3E, GNLY, and SPI1 among the myeloid cell clusters, reminiscent of a previously identified T-cell receptor (TCR)

https://doi.org/10.1038/s41467-024-55038-8

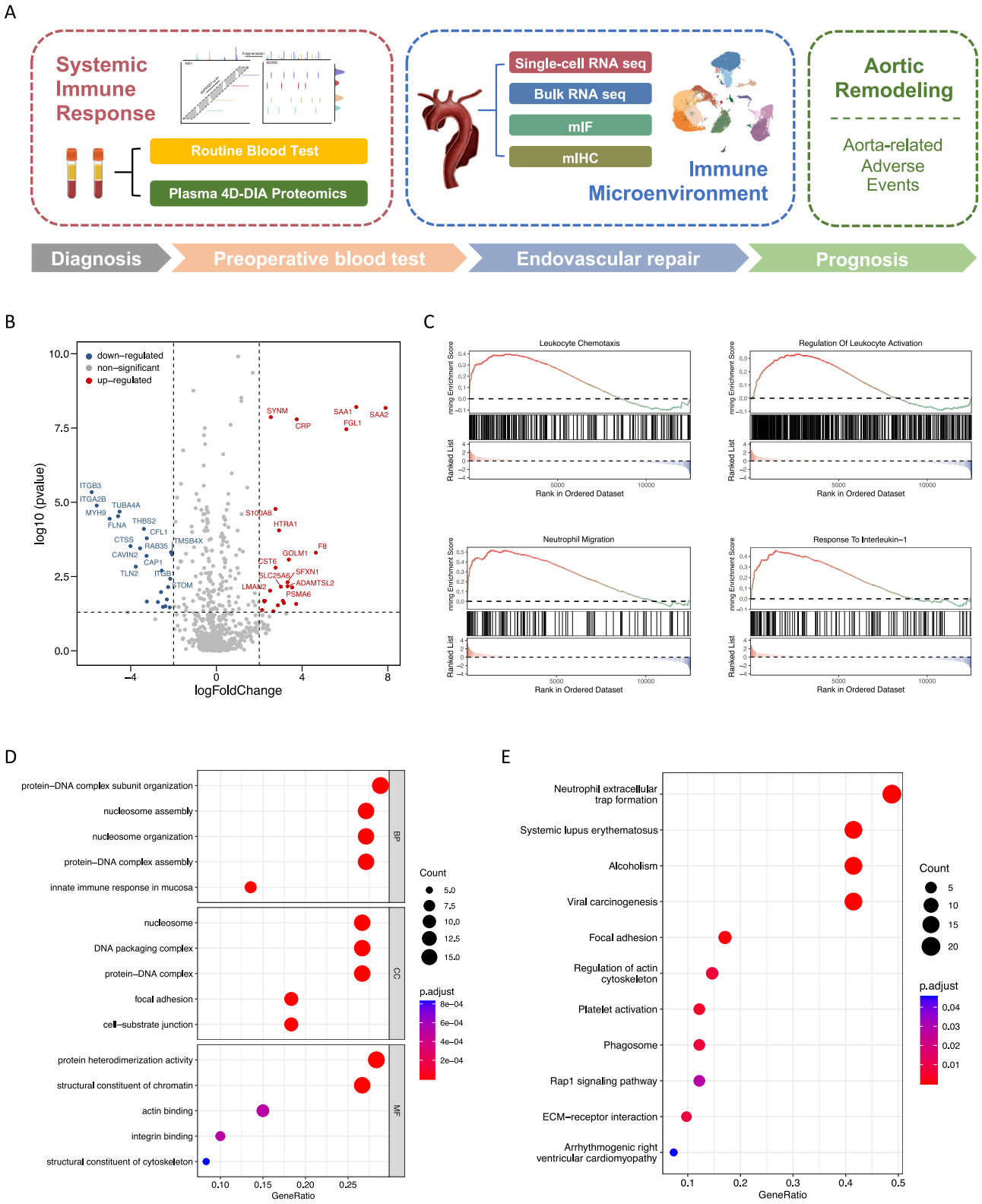

Fig. 1 | AD is marked by systemic inflammation and neutrophil activation in peripheral blood. A Flow chart of sample collection and study design. **B** Volcano plot depicting the differentially expressed proteins between patients with AD ($n = 30$) and matched healthy counterparts ($n = 30$). **C** Gene set enrichment analysis illustrating the hallmark pathways enriched in the patients with AD, including leukocyte activation and chemotaxis, neutrophil migration, and inflammatory process. **D** GO enrichment analysis showing enrichment of protein-DNA subunit organization and complex assembly, nucleosome organization and assembly in peripheral blood from patients with AD. **E** KEGG analysis showcasing enrichment pathways related to neutrophil extracellular traps (NETs) formation, platelet activation and actin regulation in peripheral blood from patients with AD. A two-sided statistical significance was set at adjusted $p < 0.05$. AD: aortic dissection; GO: Gene ontology; KEGG: Kyoto encyclopedia of genes and genomes.

https://doi.org/10.1038/s41467-024-55038-8

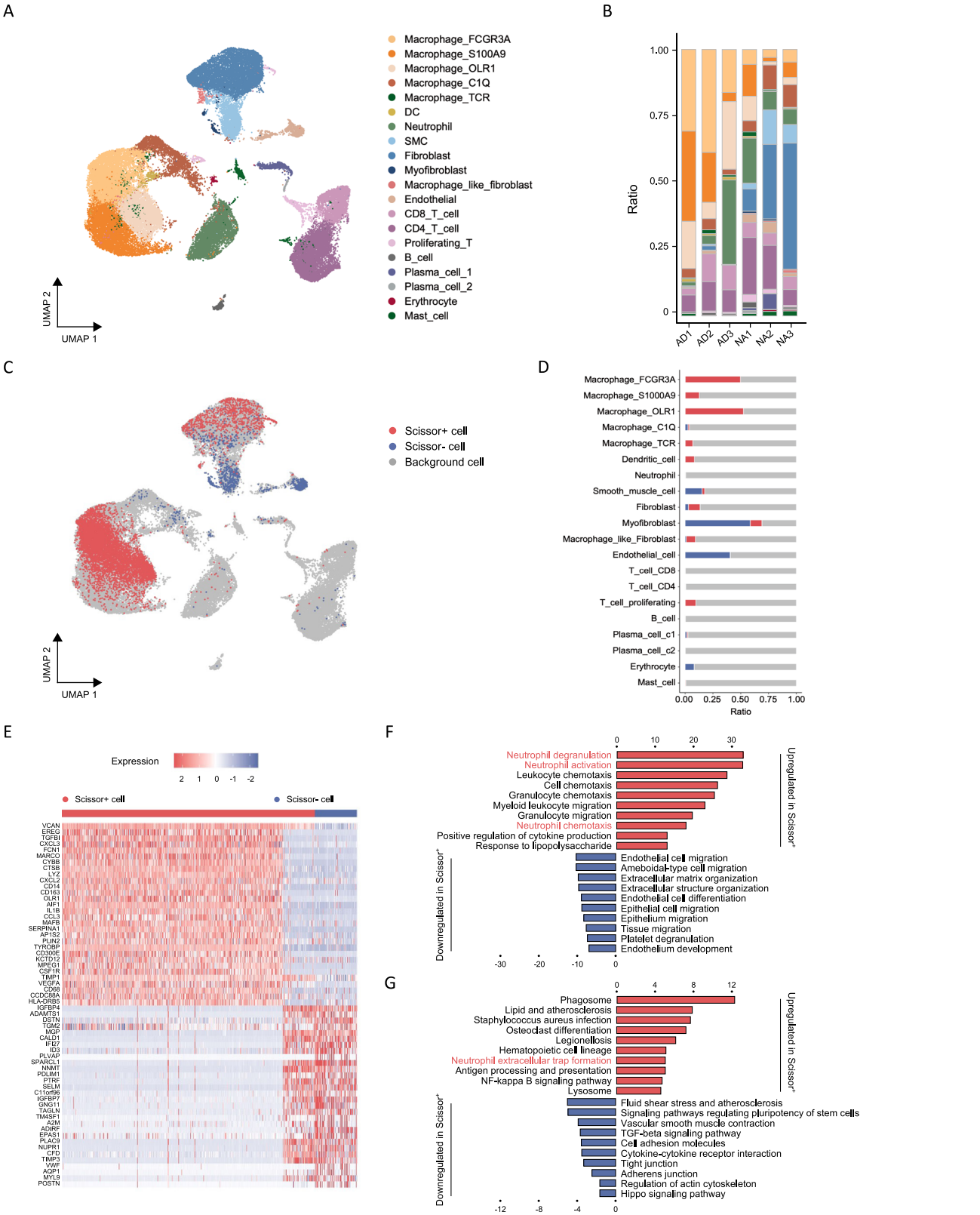

Fig. 2 | A phenotype-associated macrophage subset orchestrates neutrophil within aortic microenvironment. A UMAP representation of aligned gene expression data in single cells extracted from healthy aortas ($n = 28,428$) and dissected aortas ($n = 18,875$) showing partition into 20 distinct clusters. **B** Histogram indicating the proportion of cells in aortic tissue of each analyzed patient with AD ($n = 3$) and healthy individual ($n = 3$). **C** UMAP visualization of the Scissor-selected cells across cell populations. **D** Histogram indicating the proportion of Scissor-selected cells in aortic tissue of each analyzed patient with AD and healthy individual. **E** A heatmap plot of differential gene expressions in Scissor$^+$ cells versus Scissor$^-$ cells. **F** A bar plot of the GO enrichment of biological processes showing the significantly enriched pathways in Scissor$^+$ cells. **G** A bar plot of the KEGG enrichment showing the significantly enriched pathways in Scissor$^+$ cells. AD: aortic dissection; SMC: smooth muscle cell; DC: dendritic cell; FCGR3A: Fc fragment of IgG receptor 3a; S100A9: S100 calcium binding protein A9; OLR1: oxidized low density lipoprotein receptor 1; UMAP: uniform manifold approximation and projection.

αβ-based immune receptor found in subsets of macrophages within the hotspot regions of atherosclerotic lesions[29–31], and hereafter referred to as TCR$^+$ macrophages.

To identify cell subsets from single-cell data, we leveraged AD and healthy phenotypes obtained from widely used and publicly accessible bulk samples of 12 participants (GSE52093), the differently expression genes (DEGs) of which showed inflammatory signature in AD (Supplementary Fig. 3G). We employed Scissor to guide the identification process. Our expectation was that Scissor would extract cells that demonstrated the highest association with either the AD or normal phenotype in this heterogeneous single-cell dataset. Cells marked as Scissor-positive (Scissor$^+$) were anticipated to be related to the AD phenotype, whereas Scissor-negative (Scissor$^-$) cells were expected to be associated with the normal phenotype. Among the 47,303 cells across different cell types, Scissor identified 7319 Scissor$^+$ cells and 1207 Scissor$^-$ cells with high confidence (Fig. 2C). Notably, of the 7319 Scissor$^+$ cells, 6382 (87.2%) originated from patients with AD, while 1181 of the 1207 Scissor$^-$ cells (97.8%) came from normal samples (Supplementary Fig. 3H). These results indicate that Scissor can identify phenotype-associated subsets with a high degree of specificity in AD. Furthermore, among the selected Scissor cells, FCGR3A$^+$ macrophages and OLR1$^+$ macrophages constituted the two primary cell types, accounting for 40.6% (3464/8526) and 24.6% (2101/8526) of the total Scissor cells, respectively (Fig. 2D). SMCs and endothelial cells, on the other hand, comprised the main Scissor$^-$ cell types (Fig. 2D).

We conducted a direct comparison of the gene expression profiles between Scissor$^+$ cells and Scissor$^-$ cells to elucidate the underlying transcriptional patterns of these identified cell populations. The analysis revealed that in Scissor$^+$ cells, 148 genes were upregulated while 178 genes were downregulated when compared to Scissor$^-$ cells ($|\log2FC| > 0.5$, $p < 0.05$) (Fig. 2E). Among the upregulated genes observed in Scissor$^+$ cells, we noted their involvement in various processes such as inflammatory and immune responses, neutrophil chemotaxis (i.e., CXCL3, CXCL2, and CCL3), cytokine production (i.e., TYROBP and IL1B), monocyte-macrophage system activation (i.e., LYZ, CD14, CSF1R, CD68, and CD163), blood vessel formation (i.e., VEGFA), and extracellular matrix remodeling (i.e., VCAN and TGFB1) (Fig. 2E). On the other hand, the downregulated genes in Scissor$^+$ cells included those related to platelet adhesion and hemostasis (i.e., VWF), complement system activation (i.e., CFD), smooth muscle differentiation and contraction (i.e., TAGLN, MYL9 and CALD1), actin binding (i.e., DSTN), as well as cell-cell and cell-matrix adhesion (i.e., MGP, IGFBP4, and IGFBP7) (Fig. 2E).

To investigate the potential functional heterogeneity of the Scissor$^+$ phenotype-associated cells identified in dissected aortas, we conducted Gene Ontology (GO) term analyses. The results revealed that Scissor$^+$ cells exhibit distinct characteristics, including leukocyte chemotaxis and migration, with a particular emphasis on neutrophil activation, chemotaxis, and degranulation. Additionally, positive regulation of cytokine production, extracellular matrix structure degradation, endothelial cell differentiation, and migration were also observed (Fig. 2F). These findings are consistent with the previously identified molecular hallmarks of AD. In addition, by functional enrichment analysis using the Kyoto Encyclopaedia of Genes and Genomes (KEGG) we found that Scissor$^+$ cells may be involved in processes such as NETosis, lipid and atherosclerosis regulation, antigen processing and presentation, NF-kappa B signaling pathway, inhibition of complement and coagulation cascade, TGF-β signaling pathway inhibition and impaired vascular smooth muscle contraction in AD (Fig. 2G).

Collectively, the above results indicated that patients with AD exhibited a disordered aortic immune microenvironment, marked by the presence of phenotype-associated macrophages. These macrophages appeared to contribute to the recruitment of neutrophils through the CXCL3/CXCR2 neutrophilic chemotactic axis, possibly leading to NETosis within the dissected aorta.

Neutrophil heterogeneity and differentiation trajectories

The functional enrichment of neutrophils within AD and their close association with phenotype-associated macrophages led us to further examine neutrophils. A total of 4668 neutrophils were divided into 5 subsets that exhibited moderate tissue separation (Supplementary Fig. 4A). We proceeded to investigate the expression of CXCR1/2 in neutrophils. We found two subsets of neutrophils highly expressed CXCR1/2, CXCR4$^+$ neutrophil, and S100A12$^+$ neutrophil (Supplementary Figs. 4A, 5I), and are also positively correlated to inflammation activation (i.e., interleukin 1 receptor activity, inflammasome complex, and neutrophil degranulation), innate immune response (i.e., toll-like receptor signaling and complement activation), smooth muscle cell apoptosis (i.e., reactive oxygen species response), and angiogenesis (i.e., VEGF signaling) (Supplementary Fig. 4B). While the functions of inflammation regression and tissue repair enrich in NABP1$^+$ neutrophil and MGP$^+$ neutrophil, suggesting the two subsets might play a role in dampening excessive inflammation and protecting aorta from further severe inflammatory cascade and damage. While ANXA1$^+$ neutrophil exhibited quiescent phenotype that promote T cell proliferation, and inhibit mast cell chemotaxis and activation, playing a potential role in inducing chronic inflammation (Supplementary Fig. 4B).

Combined with differentiation hierarchies that S100A12$^+$ neutrophil showed less differentiation level (Supplementary Fig. 4C, D), differentiation trajectory analysis revealed a highly overlapping at the starting point while bifurcating at the endpoint differentiation path from S100A12$^+$ neutrophil to CXCR4$^+$ neutrophil and ultimately two subsets of MGP$^+$ pro-inflammatory and ANXA1$^+$ anti-inflammatory neutrophil, respectively (Supplementary Fig. 4E). We then proceeded to find genes that change their expression over the course of neutrophil development with a general additive model using a negative binomial noise distribution to model the relationship between gene expression and pseudotime. The S100A12 was the most dynamically expressed gene (Supplementary fig. 4F), suggesting its possible value in evaluating heterogeneous differential states. Along the trajectory by Monocle, we also identified that the pathways activated in neutrophil (i.e., CXCL8, CXCR4, CCL3, SPP1, and S100A11) were enriched at the starting point while improved resistance to stress (i.e., HSP90AB1, HSP90AA1 and CYP4F3) were enriched at the late stage resolution phase of inflammation (Supplementary Fig. 4G, H).

The results illustrated divergent neutrophil phenotypes and bifurcating differentiation trajectories in this acute inflammatory condition, wherein neutrophils demonstrated a dual nature and bipotent function, encompassing both naïve pro-inflammatory and anti-inflammatory profiles. Focusing on pro-inflammatory subsets might facilitate targeted therapeutic interventions that can either bolster the host's immune response or restore immune homeostasis, thus presenting promising avenues for ameliorating the pathological burden of AD.

Elevated NETosis occurs in aortic lesion and peripheral blood from patients with AD

We then further investigated the role of NETosis in the development of AD. Initially, we examined the expression levels and variations of NETs in aortic tissue samples obtained from individuals with AD and healthy controls. To investigate the association between NETs and different cell subgroups, we calculated the NETs-associated gene module scores[32] for both dissected and normal aortas using single-cell data. Notably, we observed a significant increase in NETs scores within the dissected aorta compared to the normal aorta. Furthermore, among the 20 cell subgroups analyzed, the highest NETs scores in neutrophils were observed (Fig. 3A).

We proceeded to determine the presence of NETs formation in human AD tissue samples. We collected a total of 4 dissected aortic tissues from patients who underwent open surgery, as well as 4 healthy

https://doi.org/10.1038/s41467-024-55038-8

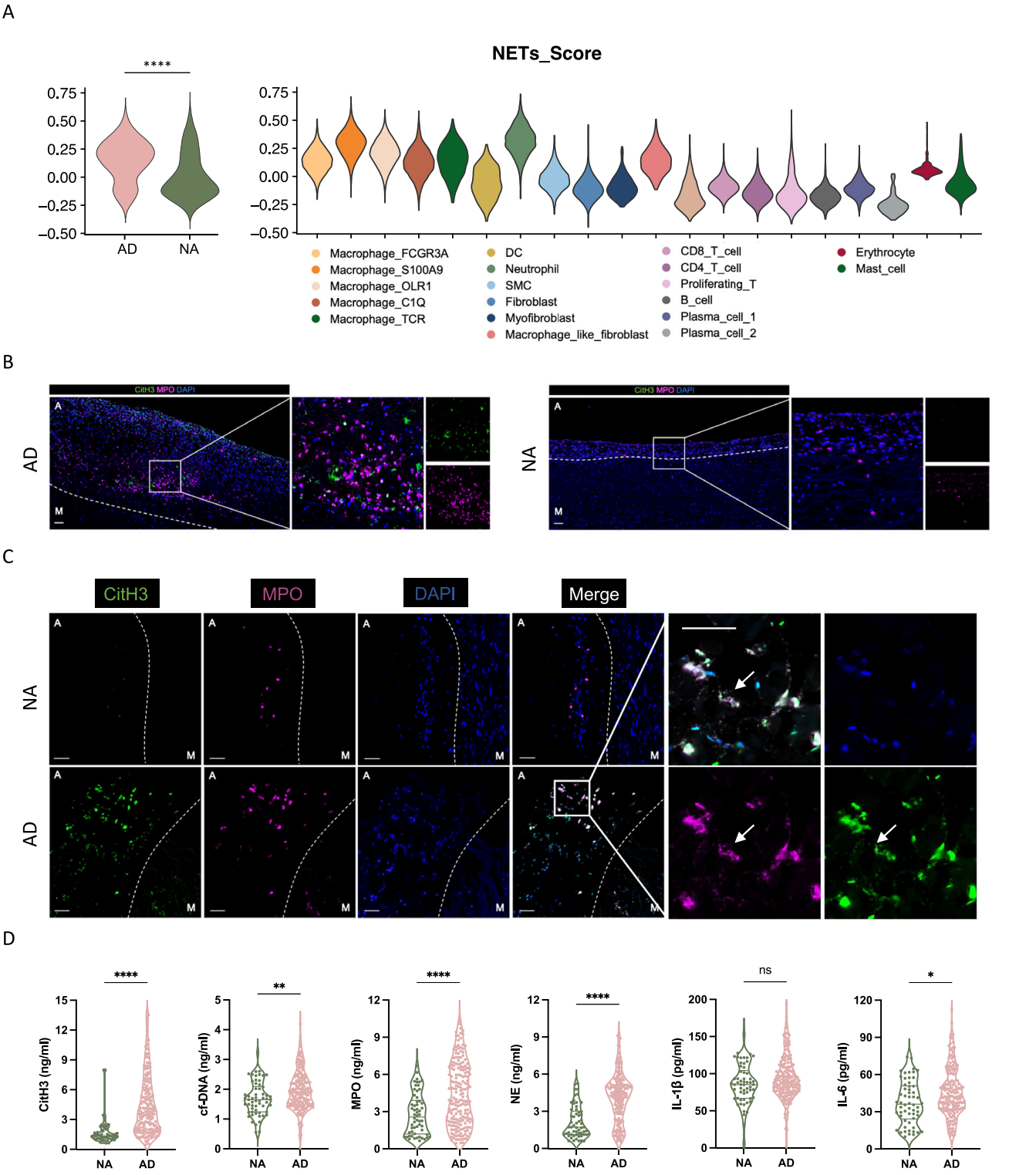

Fig. 3 | Elevated NETosis occurs in aortic lesions and peripheral blood from patients with AD. A Single-cell sequencing data of NETs-associated gene module score of dissected aortas (left) and NETs-associated gene module score of each cell cluster (right). **B** Representative immunofluorescence images of NETs identified by co-localization of MPO (red) and CitH3 (green). Scale bars = 1 mm. **C** Zoom-in immunofluorescence images of NETs determined by co-staining of MPO (red) and CitH3 (green). Scale bars = 100 μm. M indicated media, A indicated adventitia, and the white dotted line indicated the boundary between media and adventitia. **D** NETs associated markers as detected by ELISA in the plasma from patients with AD ($n = 187$) and healthy individuals ($n = 59$) ($p < 0.001$; $p = 0.0069$; $p < 0.001$; $p < 0.001$; $p = 0.2177$; $p = 0.0140$, respectively). Source data are provided as a Source Data file. Values are expressed as means ± SD. A two-sided statistical significance was set at $^{*}p < 0.05$, $^{**}p < 0.01$, $^{***}p < 0.001$, $^{****}p < 0.0001$ by Mann–Whitney *U* test. NETs: neutrophil extracellular traps; CitH3: citrullinated histone H3; cf-DNA: cell-free DNA; MPO: myeloperoxidase; NE: neutrophil elastase; IL-1β: interleukin-1β; IL-6: interleukin-6.

aortic tissues from multi-organ donors. We adopted a combination of citrullinated histone H3 (CitH3) and myeloperoxidase (MPO) to detect NETs in aortic samples. High-magnification images obtained through hematoxylin and eosin (H&E) staining displayed longitudinal sections of both dissected and normal aortas (Supplementary Fig. 6D). Representative multiplex immunohistochemical staining of a dissected aorta revealed the presence of abundant NET formations, marked by areas positive for CitH3, which largely overlapped with MPO-positive regions, specifically found in the adventitial layer of the aortic wall (referred to as "A"), rather than the medial layer of the aorta (referred to as "M"). In contrast, limited areas positive for CitH3 were observed in tissues obtained from the healthy aorta (Fig. 3B).

We subsequently quantify the presence of CitH3 in plasma samples obtained from patients with AD. We detected NETs-associated markers in the plasma from 187 patients with AD and 59 healthy individuals (Supplementary Table 2). Our findings revealed that the levels of plasma NETs markers, including CitH3, cell-free DNA (cf-DNA), MPO, NE, and IL-6, were significantly higher in patients with AD than those observed in healthy subjects (Fig. 3C and Supplementary Table 3).

These results show that the expression level of NETs in aortic lesions and peripheral blood of patients with AD were both evidently increased compared with that of healthy individuals, suggesting that NETs are involved in the occurrence and development of AD.

Inhibition of NETosis ameliorates dissection progression in AD mice

We further investigated the potential of inhibiting NETosis to alleviate or even reverse aortic lesions and improve survival. The administration of β-aminopropionitrile (BAPN) in mice was used to mimic facets of AD in human. The mechanistic basis for BAPN-induced aortopathy was proposed to be the inhibition of lysyl oxidase (LOX) activity, which catalyzed crosslinking of lysine residue in elastin and collagens to form desmosine. Two drugs Cl-amidine (PAD4 inhibitor[33]) and DNase I were adopted to inhibit NETs formation and digest NETs after their formation, respectively. The mice in the experimental group were harvested after 4-week induction of BAPN to observe the subsequent AD occurrence or immediately after death (Fig. 4A). At the end of the 4-week period, it was observed that 66.7% (8/12) of the mice developed AD in the BAPN group and 50% (6/12) of them died of aortic rupture, with the first mouse succumbing on the 9th day. In Cl-amidine group, 50.0% (6/12) of the mice developed AD and 16.7% (2/12) of them died of aortic rupture before the end of the experiment, showing Cl-amidine-treated mice had significantly less AD rupture rate and improved survival rate (Fig. 4B, C). While in DNase I group, 66.7% (8/12) of the mice developed AD and 50.0% (6/12) of them died of aortic rupture, which showed a moderate improvement in survival rate (Fig. 4B, C). Whereas the combined group of Cl-amidine and DNase I (Combo) group showed an incidence of 50.0% (6/12) and mortality of 16.7% (2/12) due to aortic rupture (Fig. 4B).

Baseline aortic diameters of each mouse were measured by vascular ultrasound at day 7 before the administration of NETs inhibitors, and no significant difference was observed among groups (Supplementary Fig. 6A, B). Of note, we happened to notice two mice with enlarged section located in proximal descending aorta in BAPN group and in combination treatment group (Supplementary Fig. 6C).

There was strong evidence of aortic expansion, elastin degradation and thrombosis in the false lumen, resulting in the compression of the true lumen, in BAPN-induced AD mice (Fig. 4G, J). Abundant staining of CitH3 and moderate staining of Ly6G were observed in AD mice (Supplementary Fig. 6E). Moreover, the average max aortic diameter, overall thickness and media thickness of aortas, and elastic fiber degradation of mice from Cl-amidine-treated and Combo group were significantly reversed compared to AD mice, suggesting reduced aortic expansion and maintained elastin integrity (Fig. 4F–I). The average max diameter of aortas from DNase I-treated mice showed a slight reduction, but without statistical significance when compared to AD mice (Fig. 4F–I).

The expression of CitH3 originating from neutrophils was confirmed by double staining for neutrophil-specific protein Ly6G, and thereby confirmed the occurrence of NETs formation in aorta from AD mice (Fig. 4K). Both Cl-amidine-treated and DNase I-treated group (Combo) demonstrated a substantial reduction in CitH3 and Ly6G or MPO positive areas when compared to BAPN-induced AD mice (Fig. 4K).

Taken together, our findings suggested that alleviating the progression and rupture of AD in mice can be achieved by inhibiting NETs formation through the blockade of histone citrullination, while inhibiting NETs function via DNase I treatment is not as effective.

Macrophage fosters NETs formation via CXCL3/CXCR2 axis

We proceeded to investigate the cell-cell communication mechanisms within all clusters, with a particular focus on understanding the molecular interactions involved in phenotype-specific macrophages and their potential interaction with targeted neutrophil populations. To achieve this, we evaluated the putative crosstalk by examining the expression and downstream targets of ligand-receptor pairs, particularly those concerning neutrophils (Fig. 5A). We found that FCGR3A$^+$ macrophages and OLR1$^+$ macrophages, which comprised most of the phenotype-specific macrophages, exhibited strong interactions with other macrophage populations, fibroblasts, macrophage-like fibroblasts and neutrophils (Supplementary Fig. 5A, B). Notably, the most significant increases on the paired CXCL3/CXCR2 pathways originating from macrophages to neutrophils were observed (Fig. 5B).

Next, we found that expression of CXCL3 was higher in AD than in normal aorta (Supplementary Fig. 5C), and phenotype-associated macrophages, especially FCGR3A$^+$ macrophages and OLR1$^+$ macrophages, displayed elevated expression compared to other clusters (Supplementary Fig. 5D, E). Also known as growth-regulated protein-gamma (Gro-gamma), CXCL3 is a prominent neutrophil-activating chemokine belonging to the GRO subfamily of CXC chemokines[34]. Its functional receptor in neutrophils is CXCR2, which facilitates neutrophil arrest. The protein encoded by CXCL3 binds to receptors encoded by CXCR2 and CXCR1 on neutrophils, indicating that FCGR3A$^+$ macrophages and OLR1$^+$ macrophages can directly engage with neutrophils through adhesive ligand-receptor pairs, putatively CXCL3-CXCR2 pathways.

We proceed to delve into the role of CXCL3-CXCR2 pathways during NETs formation in AD. Thereby, though immunofluorescence imaging of both patient- and mouse-derived tissue, we confirmed the prevalent existence of CXCL3$^+$ macrophages and CXCR2$^+$ neutrophils within the human dissected aortas (Fig. 5C, E), as well as in the mice dissected aortas (Fig. 5D, F). Correlation analysis also showed that the number of CXCL3$^+$ macrophages was positively correlated with the number of CXCR2$^+$ neutrophils in a statistically significant manner (Fig. 5G). We also found the positive correlation between elastin degradation grading and CXCL3$^+$ macrophages (Fig. 5H) and CXCR2$^+$ neutrophils, respectively (Fig. 5I).

We further proceeded to verify the role of CXCL3/CXCR2 axis in NETs formation through mice model (Fig. 6A). At the end of the 4-week period, there was 50.0% (6/12) of the mice in the BAPN plus IgG group succumbing due to aortic rupture. In contrast, the mortality rate due to aortic rupture in the anti-CXCL3 group was 25.0% (3/12), while in the anti-CXCR2 group it was 16.7% (2/12) (Fig. 6B). The survival analysis showed improved mortality due to aortic rupture in anti-CXCL3 and anti-CXCR2 groups (Fig. 6C). Moreover, significant reversal of the average max aortic diameter, overall and media thickness, elastic fiber degradation, and NETs marker presence were observed in anti-CXCL3 and anti-CXCR2 groups (Fig. 6D–K and Supplementary Fig. 6F). In

https://doi.org/10.1038/s41467-024-55038-8

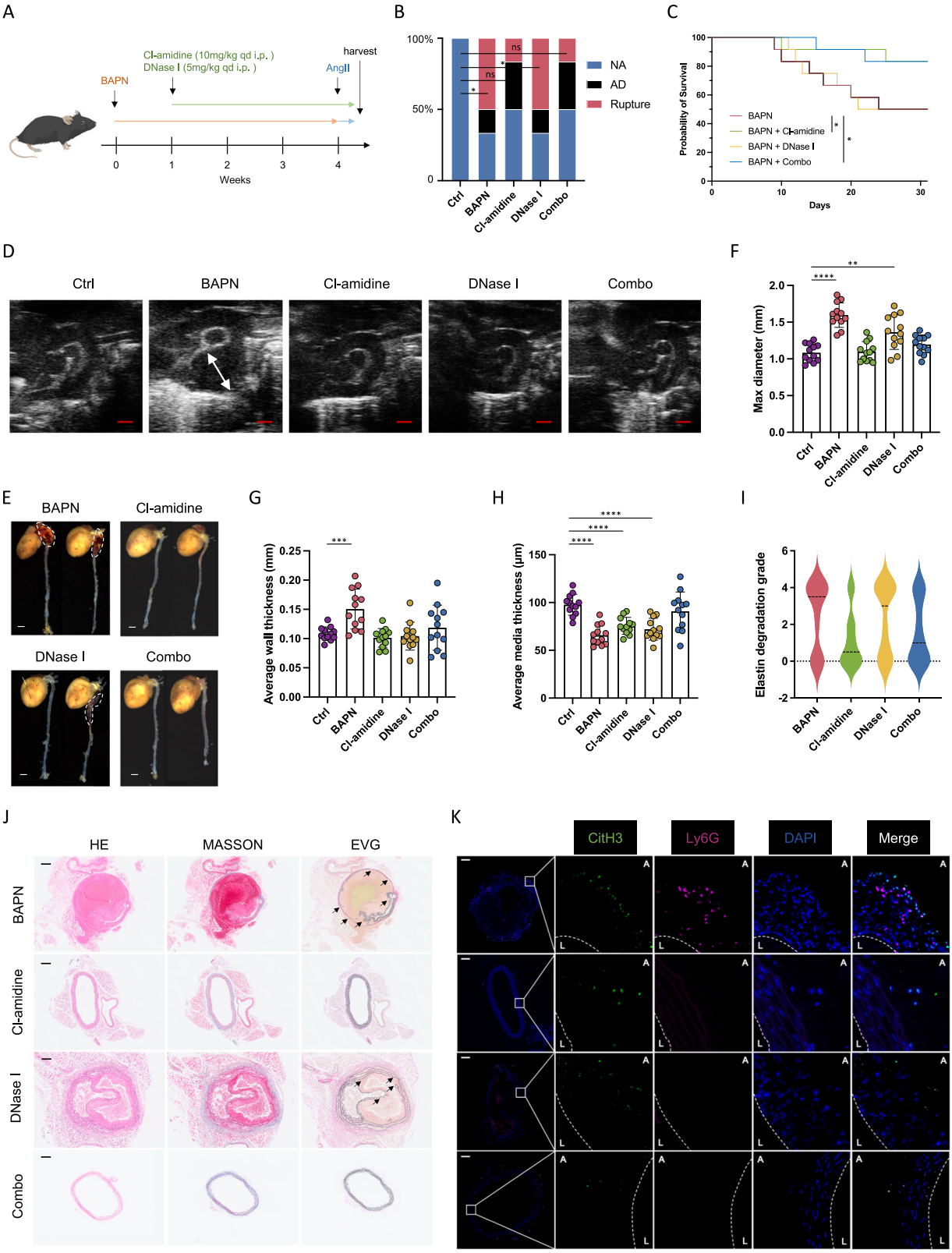

addition, we quantified immunofluorescence of NETs markers among four elastin degradation grades, and the results showed a gradually higher NETs level along with the increasing degree of elastic fiber degradation.

These findings suggested that the CXCL3/CXCR2 axis plays a crucial role in the macrophage-neutrophil interaction, thereby contributing to the progression and rupture of AD.

NETs-associated markers serve as prognostic risk factors

The findings from our experiments conducted on human and mice aortic tissue strongly suggest the involvement of NETs in the development of AD. This further highlights their potential for predicting and assessing the prognosis of AD. To investigate this further, we categorized patients into two groups based on whether they experienced postoperative aorta-associated adverse events (AAEs). The expression

Fig. 4 | Inhibition of NETosis attenuates dissection progression in mice with AD. **A** Schematic overview of experimental design. Each mouse received intraperitoneal injection of saline, Cl-amidine (10 mg/kg), DNase I (5 mg/kg) or both drugs at a fixed time once a day during 4–7 weeks of age until death or the end point of the experiment. **B** The incidence of AD and aortic rupture in each group ($n = 12$). Comparisons by Fisher's exact test indicating aortic rupture rate difference among groups ($p = 0.0137$; $p = 0.4783$; $p = 0.0137$; $p = 0.4783$). **C** Mice death due to aortic rupture of each indicated group ($n = 12$) ($p = 0.0378$ for Cl-amidine vs BAPN; $p = 0.0424$ for Combo vs BAPN). **D** Representative vascular ultrasound images of aorta in each group ($n = 12$). Scale bar = 1 mm. **E** Representative macrographs of aortas in each group. Scale bar = 20 mm. **F** The average of max diameter (**F**) ($p = 0.0018$ for DNase I vs Ctrl), aortic wall thickness of aortas (**G**) ($p < 0.0006$ for BAPN vs Ctrl), and media thickness (**H**) in each group ($n = 12$). **I** Elastin degradation grading evaluation of aorta in each group ($n = 12$) ($p = 0.0337$ for Cl-amidine vs BAPN; $p = 0.0436$ for Combo vs BAPN). **J** Representative immunohistochemistry images showing aortic dilation, false lumen formation, and elastin degradation within aortas in each group. Arrow indicating broken elastin. (K) Representative immunofluorescence images showing NETs formation within aortas of mice, determined by CitH3 (citrullinated histone H3, green) and neutrophil (Ly6G, red) staining. Scale bar = 100 μm. Values are expressed as means ± SD. A two-sided statistical significance was set at $^{*}p < 0.05$, $^{**}p < 0.01$, $^{***}p < 0.001$, $^{****}p < 0.0001$ by Mann–Whitney *U* test or Fisher's exact test. Log-rank test was used for the analysis of survival rate.

levels of NET markers in the plasma of patients who underwent endovascular treatment were measured separately for those with and without AAEs. In a prospective cohort study, 116 patients were closely monitored through blood tests and computed tomography angiography (CTA) during a mean (±SD) follow-up period of 20.5 (±16.8) months. Out of the total patients, 31 developed AAEs while the remaining 85 patients remained stable throughout the follow-up period. The baseline characteristics of patients were shown (Supplementary Table 4). The patients with AAEs exhibited significantly higher levels of CitH3 and MPO compared to those without AAEs (Fig. 7A).

Using the maximally selected log-rank statistic, a cut-off level of 6.91 ng/mL was determined (Supplementary Fig. 6I) to predict the occurrence of AAEs in patients with AD. The sensitivity and specificity of this cut-off level were found to be 0.6 and 0.9, respectively, with an area under the curve (AUC) value of 0.751 (Fig. 7B). Notably, among patients with high levels of CitH3 (≥6.91 ng/ml), 70.37% (19 out of 27) developed AAEs, while 86.36% (76 out of 88) of patients with low levels of CitH3 (<6.91 ng/ml) did not experience AAEs (Fig. 7C).

Both the Least Absolute Shrinkage and Selection Operator (LASSO) and multivariable Cox regression models demonstrated that CitH3 and IL-1β were independent risk factors associated with a poor prognosis in patients with AD (HR 8.78, 95% CI 3.82-20.16, $p < 0.001$; HR 3.04, 95% CI 1.01-9.17, $p = 0.048$) (Fig. 7D). To reduce the potential bias, we then reanalyzed the prognostic value of NETs associated markers with previously reported risk factors including D-dimer, NLR, SIRI. We found that when competing with previously established predictors, CitH3 still exhibited good predictive accuracy with HR of 1.18 (95%CI 1.05-1.33) and *p*-value of 004 after adjusting the confounding factors in the multivariable analysis (Supplementary Table 5). Moreover, Kaplan–Meier curves revealed that patients with elevated levels of CitH3 had a higher occurrence of AAEs compared to those with lower levels of CitH3 (Fig. 7E). Additionally, patients with high IL-1β (≥90.86 pg/ml) also displayed a greater incidence of AAEs compared to patients with low IL-1β levels (<90.86 pg/ml) (Fig. 7F). We also combined CitH3 and IL-1β into one group to see their predictive accuracy in combination. Both patients of high CitH3 and high IL-1β, and high CitH3 or high IL-1β yielded statistically significant differences and diverged survival curves (Supplementary Fig. 6J, K). Collectively, CitH3 was identified as an independent risk factor for AAEs following endovascular treatment of AD.

Discussion

Our study provides a comprehensive transcriptomic landscape of aortic lesions at a single-cell resolution, as well as the proteome profiling of peripheral blood cells from AD patients compared to healthy individuals. This integrated multi-omics analysis identified the highly phenotype-associated macrophage populations, which dovetailed with previous studies on atherosclerosis that suggested that pathogenic macrophages originate from tissue-resident macrophages and newly recruited monocytes, which subsequently differentiate into macrophages[26,35]. Our data indicate that the increase in the number of macrophages was mostly due to an expansion of inflammatory macrophages, atherosclerosis-like foamy macrophages and MDSCs-like macrophages, suggesting that macrophage phenotype switching may occur in the dissected aorta.

The inflammatory macrophages identified in our analysis exhibited a gene expression profile of prototypical proinflammatory macrophages, characterized by high expression of chemokines and cytokines. They also showed enrichment of CD163, a marker of the classic M2 anti-inflammatory phenotype. Similarly, MDSCs-like macrophages displayed increased expression of the S100A family genes including S100A8, FCN1 and VCAN, resembling the gene expression patterns of pathologically activated monocytes and neutrophils with immunosuppressive activity during inflammation and infection[36]. However, these macrophages further triggered leukocyte recruitment, degranulation, and NETs formation[37].

Tissue-resident macrophages exhibiting highly expression of C1QA, C1QB and C1QC play controversial roles in cardiovascular diseases. Elevated level of C1Q was demonstrated to cause atherosclerosis directly in vitro and in vivo in mice, which has been linked to the severity and extent of atherosclerosis in human[38]. Conversely, C1Q highly-expressing macrophages with an anti-inflammatory phenotype was identified to alleviate inflammation in atherosclerotic lesions[39,40]. These seemingly dichotomous and ambivalent features could make sense from an evolutionary perspective: the feedback inhibition pathways of inflammation are activated among inflammatory macrophages, thereby curtailing overwhelming activation, self-propagating inflammatory cascades, and facilitating restoration of tissue homeostasis in dissected aortas[41].

Increasing evidence suggests a role for OLR1 in miscellaneous steps of the atherosclerotic process, from initiation to plaque destabilization[42]. The existence of these atherosclerosis-like foamy macrophages that we observed in the dissected aorta indicates the similarity of pathologic mechanisms between atherosclerosis and AD. However, the patterns of atherosclerosis susceptibility are considerably influenced by intrinsic discrepancies in the artery wall cells located differently within the vascular system, in which the thoracic aorta is an atherosclerosis-resistant segment[43]. This may illustrate the overlapping gene expression pattern and functional enrichment between $OLR1^{+}$ macrophages in our study and the previously uncovered subset of aortic $TREM2^{+}$ macrophages in mouse models of atherosclerosis, which additionally expressed a high level of LGALS3, CD72 and HEXB[26]. Further investigation of the function of genes exclusively expressed in atherosclerosis-like foamy macrophages in dissection but not in atherosclerosis may shed light on the accurate role of these cells and the concrete mechanisms in control of their differentiation and function in the aortic wall.

Integrating external phenotypic information from bulk data to guide single-cell data analysis enables the identification of disease-relevant macrophage subset, which predominantly consisted of inflammatory macrophages and atherosclerosis-like macrophages, suggesting their close association with the dissection phenotype and the important role of the CXCL3-CXCR2 neutrophilic chemotactic axis in disease progression. Previous study pinpointed the macrophage

https://doi.org/10.1038/s41467-024-55038-8

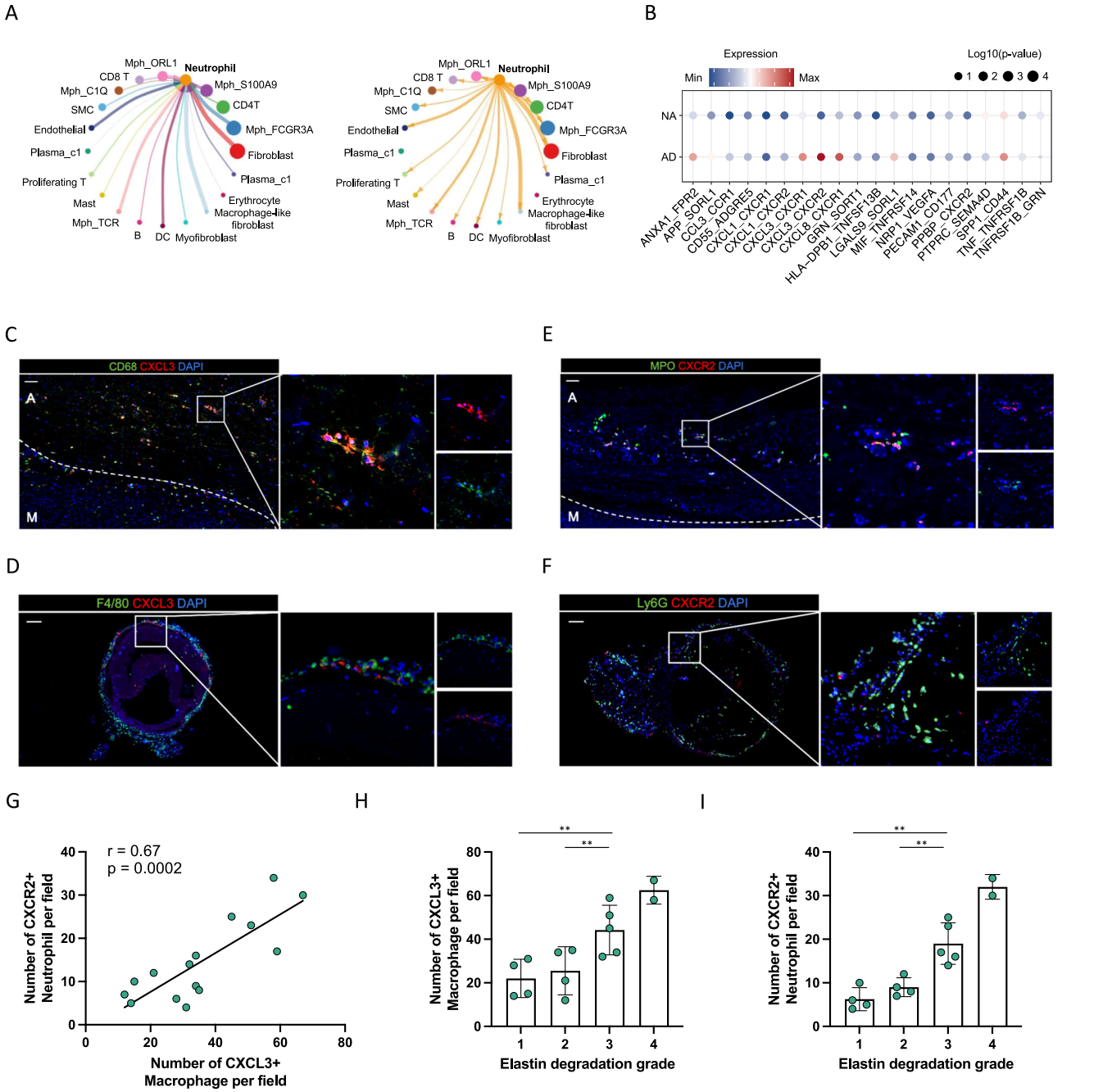

Fig. 5 | CXCL3⁺ macrophages were positively correlated with CXCR2⁺ neutrophils within AD lesion. A Interaction network of main cell types in AD constructed with CellChat. **B** The ligand-receptor interactions between macrophages and neutrophils in AD compared to those in NA. **C**, **D** Representative images of the presence of CXCL3⁺ macrophages within human (**C**) and mice (**D**) dissected aorta. Scale bars = 100 μm. **E**, **F** Representative images of the presence of CXCR2⁺ neutrophils within human (**E**) and mice (**F**) dissected aorta. Scale bars = 100 μm. **G** Pearson correlation analysis showing positive linear correlation between the number of CXCL3⁺ macrophages and the number of CXCR2⁺ neutrophils within human aortic lesion ($n = 5$, three fields per sample). **H**, **I** Bar plot showing the positive correlation between elastin degradation grading and CXCL3⁺ macrophages (**H**) and CXCR2⁺ neutrophils (**I**) ($n = 5$, three fields per sample). Values are expressed as means ± SD. A two-sided statistical significance was set at $^{*}p < 0.05$, $^{**}p < 0.01$, $^{***}p < 0.001$, $^{****}p < 0.0001$ by Mann–Whitney *U* test.

subset as the predominant origin of detrimental molecules for aneurysm and AD, including IL1RN/TREM1 M1-like macrophage subcluster, which also expressed high levels of proinflammatory chemokines such as CXCL2, CCL3, and CCL4[44,45]. While our study uncovered the macrophage subcluster that highly expressing inflammatory chemokines and cytokines, but moderately expressing of TREM1 and IL1RN, which further indicates the intrinsic difference in the underlying pathologic mechanism between aneurysm and dissection. Recently, CXCL3⁺ inflammatory macrophages have been detected primarily in acute coronary culprit plaques rather than in chronic plaques, exhibiting potential therapeutic targets for preventing acute coronary syndrome[46]. Likewise, to further contextualize our findings, it would be interesting to test the effects of specific depletion of CXCL3⁺ macrophage in an AD mouse model.

Similar to what is observed in macrophages, neutrophil accumulation has been proven to produce various inflammatory signals that amplify leukocyte recruitment and perpetuate inflammation, thereby promoting tissue destruction[47,48]. However, a recent study

https://doi.org/10.1038/s41467-024-55038-8

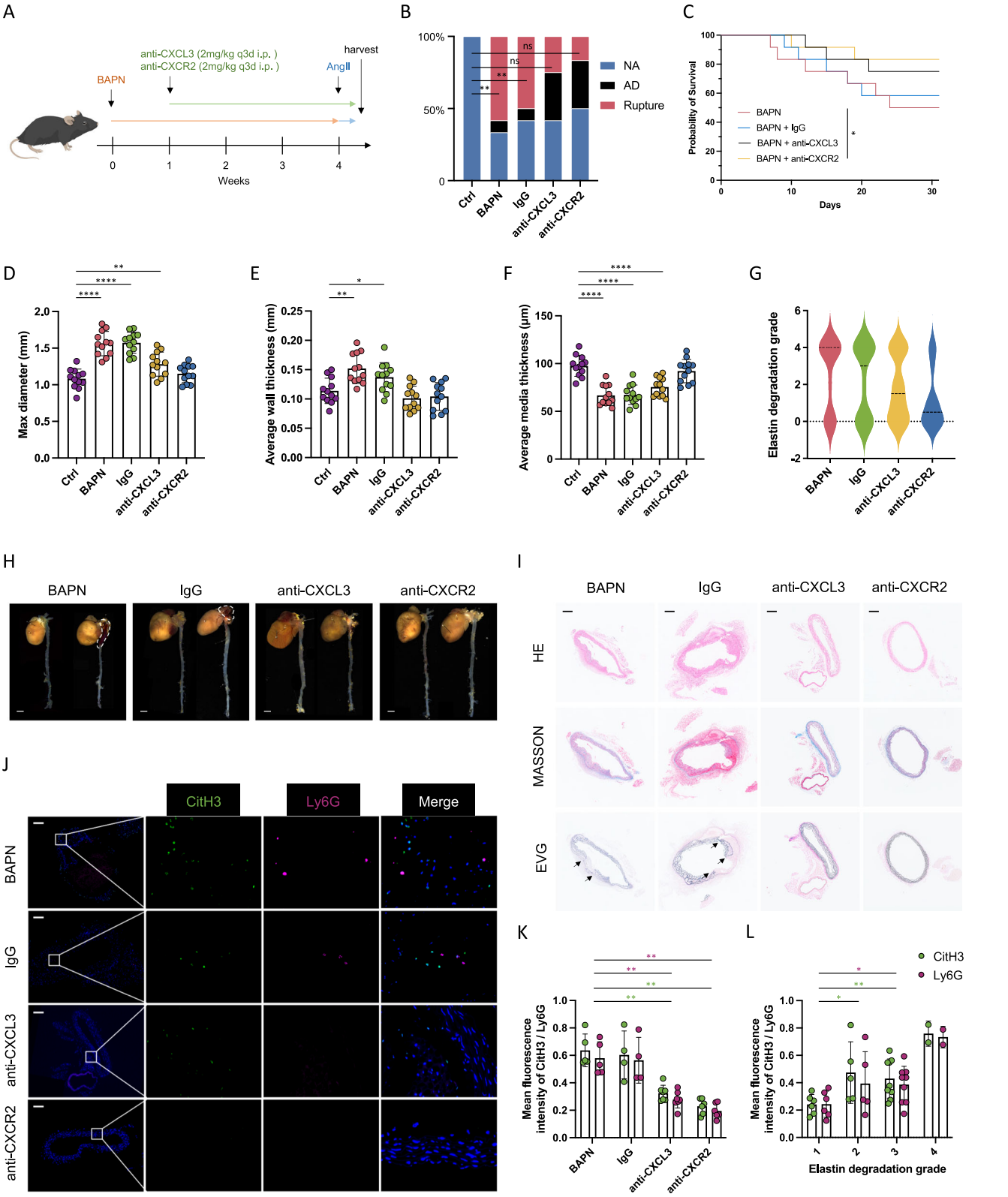

demonstrated that neutrophils and neutrophil-derived lipocalin production can trigger the recruitment of circulating monocytes, induce clearance of debris and enable resolution of inflammation and proper wound healing in the context of acute myocardial healing[49]. It remains to be investigated whether these opposite outcomes of neutrophil activity are a consequence of neutrophil subsets exerting contradictory functions, or if their action is dictated in a context-dependent manner to cues within the aortic microenvironment. During the paradigm changing from reactive to predictive, preventive, and personalized medicine[50–52], such dichotomous functions of neutrophils should be taken into account when designing therapeutic drugs that target neutrophils[53].

Previous studies have demonstrated the ability of neutrophils to undergo NETosis, a process by which they produce and release NETs, which are lattices composed of DNA filaments interspersed with enzymes that effectively immobilize and eradicate bacteria[54].

Fig. 6 | Macrophage fosters NETs formation via CXCL3/CXCR2 axis. A Schematic overview of experimental design. Mice received intraperitoneal injection of IgG anti-body, anti-CXCL3 anti-body (2 mg/kg), and anti-CXCR2 anti-body (2 mg/kg) at a fixed time once a day until death or the end point of the experiment. **B** The incidence of AD and aortic rupture in each group ($n = 12$). Comparisons by Fisher's exact test indicating aortic rupture rate difference among groups ($p = 0.0045$; $p = 0.0137$; $p = 0.2174$; $p = 0.4783$). **C** Mice death due to aortic rupture of each indicated group ($p = 0.0408$ for anti-CXCR2 vs BAPN). **D**–**F** The average of max diameter (**D**) ($p = 0.0065$ for anti-CXCL3 vs Ctrl), aortic wall thickness (**E**) ($p = 0.0012$ for BAPN vs Ctrl; $p = 0.0284$ for IgG vs Ctrl), and aortic media thickness (**F**) in each group. **G** Elastin degradation grading evaluation of each aorta ($p = 0.0423$ for anti-CXCL3 vs BAPN; $p = 0.0318$ for anti-CXCR2 vs BAPN). **H** Representative macrographs of aortas in each group. Scale bar = 20 mm. **I** Representative immunohistochemistry images showing aortic dilation, false lumen formation, and elastin degradation within aortas in each group. Scale bar = 100 μm. **J** Representative immunofluorescence images showing NETs formation within aortas of mice. Scale bar = 100 μm. **K** Immunofluorescence quantification of NETs markers among each group (CitH3: $p = 0.0025$ for anti-CXCL3 vs BAPN; $p = 0.0044$ for anti-CXCR2 vs BAPN; Ly6G: $p = 0.0025$ for anti-CXCL3 vs BAPN; $p = 0.0043$ for anti-CXCR2 vs BAPN). **L** Immunofluorescence quantification of NETs markers within aortas with four elastin degradation grades (CitH3: $p = 0.0489$ for grade 2 vs grade 1; $p = 0.0012$ for grade 3 vs grade 1; $p = 0.0473$ for grade 4 vs grade 1; Ly6G: $p = 0.0537$ for grade 2 vs grade 1; $p = 0.0425$ for grade 3 vs grade 1; $p = 0.0414$ for grade 4 vs grade 1). Values are expressed as means ± SD. A two-sided statistical significance was set at $^{*}p < 0.05$, $^{**}p < 0.01$, $^{***}p < 0.001$, $^{****}p < 0.0001$ by Mann–Whitney *U* test.

However, the role of NETosis extends beyond just protection from infectious conditions, as it also contributes to autoimmune diseases, the initiation and facilitation of metastasis of malignant tumors, the progression of cardiovascular diseases, the promotion of abnormal coagulation and thrombosis, aiding in wound healing and the response to traumatic events. The role of NETs in atherosclerosis was first confirmed in 2015 that cholesterol crystals trigger neutrophils to release NETs, which in turn induce macrophages to release cytokines, activate helper T cells and amplify immune cell recruitment in atherosclerotic plaques. Interestingly, Cl-amidine failed to effectively block the formation of NETs caused by cholesterol crystals, and DNase I treatment successfully degraded NETs and eliminated downstream cytokine release, suggesting that the formation of NETs caused by hypercholesterolemia during atherosclerosis is independent of PAD enzymes and the DNA double-strand released after the formation of NETs plays an essential role in promoting inflammation and plaque progression[55]. Another study further confirmed that increased systemic NETs levels and elevated extracellular DNA levels impair serum DNase activity, described as NETs-mediated DNase response, which is essential for rapid clearance of NETs and remission of inflammation. Therefore, exogenous DNase supplementation to correct defective DNase response holds importance in plaque regression[56]. Conversely, another study found that NETs formation was detected in mice at the early stage of induced abdominal aortic aneurysm, and treatment with Cl-amidine could significantly reduce the formation of abdominal aortic aneurysm, while treatment with DNase has no effect, favouring a similar interpretation as ours in AD that the NETs formation initiates inflammatory damage in the pathogenesis of aortic disease, which may not be easily reversed once it occurs[57]. Interestingly, a considerable portion of CitH3 signal is detected without co-localization with neutrophil markers, hinting at other critical sources of extracellular trap formation in AD. While neutrophils are the primary contributors of extracellular DNA traps, other granulocytes, as well as mononuclear phagocytes and eosinophils, have also demonstrated the ability to form extracellular traps and externalize chromatin in response to various stimuli[58]. Thus, the mechanism and the potential diagnostic or prognostic role of extracellular DNA traps originating from other immune cells in AD are highly promising and warrant further exploration.

Due to the negative effects of NETs on the outcome and prognosis of the cardiovascular diseases, the level of NETs may be closely associated with the severity of the disease. A prospective, cross-sectional cohort study compared the severity, extent and phenotype of coronary atherosclerosis determined by coronary CT angiography with the expression levels of NETs-associated markers, including double-stranded DNA, nucleosomes, myeloperoxidase-DNA complexes and citrulline histone H4 in circulating blood, the first three of which were found to be positively correlated with thrombin production and significantly increased in patients with severe coronary atherosclerosis or artery calcification. Multiple regression analyses identified elevated plasma nucleosome level as an independent risk factor for severe coronary artery stenosis, and the myeloperoxidase-DNA complex predicted the number of atherosclerotic coronary vessels and the occurrence of major adverse cardiac events[59]. In addition, plasma CitH3 levels were found in a prospective aortic aneurysm cohort to predict an increase in aneurysm diameter over the next 6 months, with an area under the curve of 0.707[60]. Our study underscores the value of plasma CitH3 expression level in predicting aorta-related adverse events (AAEs) following endovascular treatment, which is of great promise for prognostic prediction and evaluation of patients with AD.

As with all sequencing studies, ours also has some limitations. Firstly, phenotype information from a single bulk dataset of 12 human subjects may skew the results, which warrants further evaluation of results in larger datasets with abundant phenotype information. Secondly, Scissor-positive cells included only a subset of neutrophils, which may be attributed to the inherent properties of neutrophils, such as their short half-life in vivo, extreme delicacy and vulnerability ex vivo, and the limitations of the 10x Chromium platform technical issues that clearly underrepresents neutrophil. Thirdly, determining exactly how NETs formation promotes inflammation and aggravates AD progression is beyond the scope of this study and require further investigation.

Methods

This study was approved by the Ethics Committee of Zhongshan Hospital of Fudan University (IRB number B2019-231R). Collection of clinical human samples. Healthy normal aortas and dissected aortas were collected from participants with written informed consent, following approval from the Medical Ethics Committee of Zhongshan Hospital, Fudan University.

Tissue dissociation and cell purification

Fresh tissues were kept in RPMI 1640 containing 10% FBS on ice immediately after retrieval from surgical intervention. Tissues were transported in sterile culture dish with 10 ml 1x Dulbecco's Phosphate-Buffered Saline (DPBS; Thermo Fisher, Cat. no. 14190144) on ice to remove the residual tissue storage solution, then minced on ice. All tissues were further processed within 3 hours. We used dissociation enzyme 0.25% Trypsin (Thermo Fisher, Cat. no.25200-072) and 10 ug/mL DNase I (Sigma) dissolved in PBS with 5% Fetal Bovine Serum (FBS; Thermo Fisher, Cat. no. SV30087.02) to digest the tissues. Tissues were dissociated at 37 °C with a shaking speed of 50 r.p.m for about 40 min. We repeatedly collected the dissociated cells at intervals of 20 min to increase cell yield and viability. Cell suspensions were filtered using a 40-um nylon cell strainer and red blood cells were removed by 1X Red Blood Cell Lysis Solution (Thermo Fisher, Cat. no. 00-4333-57). Dissociated cells were washed with 1x DPBS containing 2% FBS. Cells were stained with 0.4% Trypan blue (Thermo Fisher, Cat. no. 14190144) to check the viability on Countess® II Automated Cell Counter (Thermo Fisher).

https://doi.org/10.1038/s41467-024-55038-8

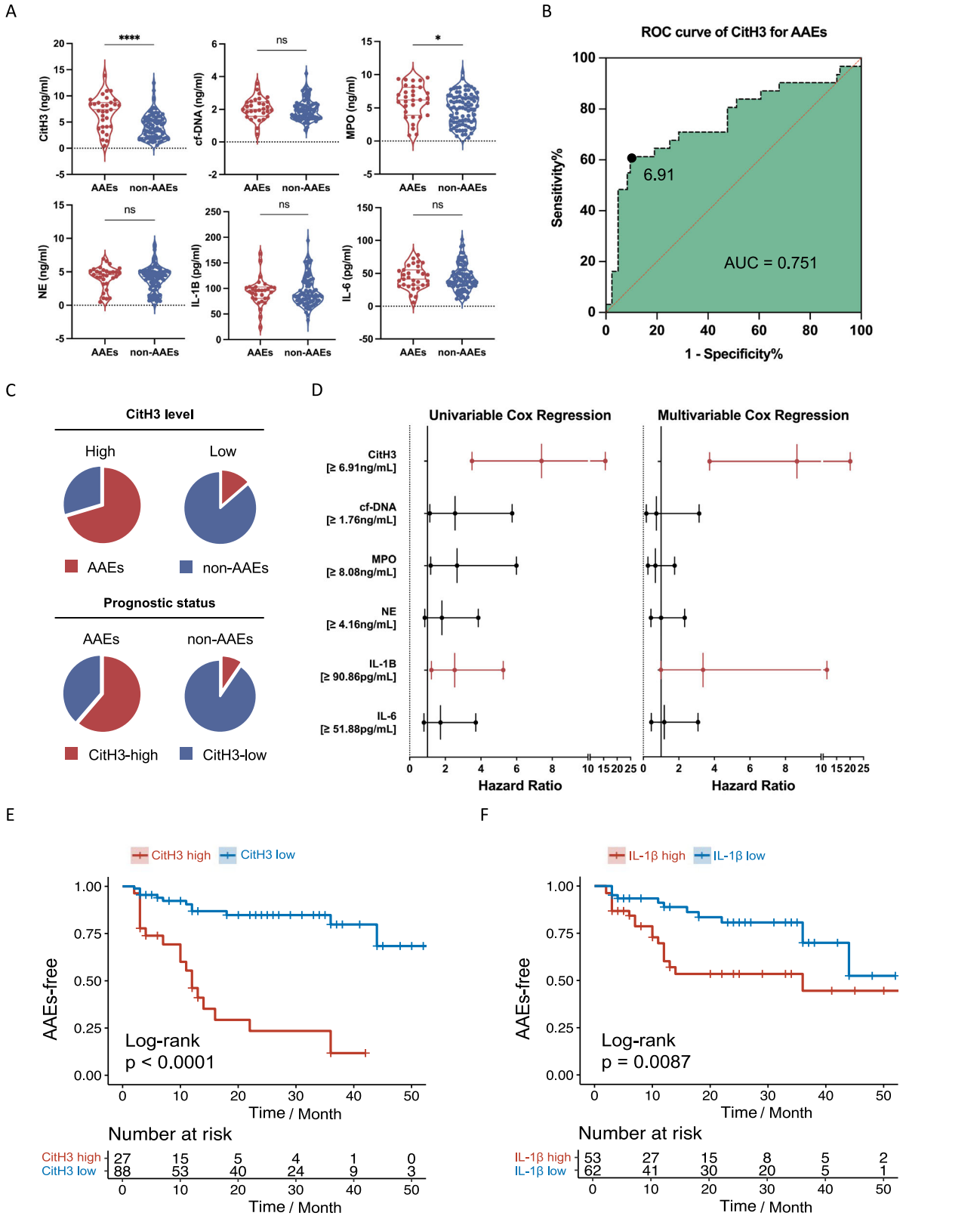

10x library preparation and sequencing Beads with unique molecular identifier (UMI) and cell barcodes were loaded close to saturation, so that each cell was paired with a bead in a Gel Beads-in emulsion (GEM). After exposure to cell lysis buffer, polyadenylated RNA molecules hybridized to the beads. Beads were retrieved into a single tube for reverse transcription. On cDNA synthesis, each cDNA molecule was tagged on the 5'end (that is, the 3'end of a messenger RNA transcript) with UMI and cell label indicating its cell of origin. Briefly, 10× beads that were then subject to second-strand cDNA synthesis, adaptor ligation, and universal amplification. Sequencing libraries were prepared using randomly interrupted whole-transcriptome amplification products to enrich the 3' end of the transcripts linked with the cell barcode and UMI. All the remaining procedures including the library construction were performed according to the standard

Fig. 7 | NETs-associated markers serve as prognostic risk factors. A The levels of NETs-associated markers in plasma of patients with ($n = 31$) or without AAEs ($n = 85$) after endovascular treatment ($p < 0.001$; $p = 0.3505$; $p = 0.0207$; $p = 0.5449$; $p = 0.5294$, $p = 0.6997$, respectively). **B** ROC curve analysis showing that at the cut-off level defined as 6.91 ng/ml CitH3, the sensitivity and specificity for predicting AAEs are 0.6 and 0.9, respectively, with the area under the curve of 0.75. **C** Pie chart displaying the frequencies for combinations of levels of CitH3 (split into categorical variable) and prognostic status (whether patients developed AAEs). **D** The univariable and multivariable Cox regression models showing that CitH3 and IL-1β were independent risk factors for AAEs of patients with AD. The upper- and lower-line segment indicating the 95% confidence interval. (E) Kaplan-Meier curves of patients with high levels of CitH3 (≥6.91 ng/ml) and the incidence of AAEs compared to patients with low levels of CitH3 (<6.91 ng/ml). Below the survival curves showing the number of exposed subjects at each time point. **F** Kaplan–Meier curves of patients with high IL-1β (≥90.86 pg/ml) and the incidence of AAEs compared to patients with low IL-1β (<90.86 pg/ml). Below the survival curves showing the number of exposed subjects at each time point. Values are expressed as means ± SD. Source data are provided as a Source Data file. A two-sided statistical significance was set at $^{*}p < 0.05$, $^{**}p < 0.01$, $^{***}p < 0.001$, $^{****}p < 0.0001$ by Mann–Whitney *U* test. ROC: receiver operating characteristic.

manufacturer's protocol (CG000206 RevD). Sequencing libraries were quantified using a High Sensitivity DNA Chip (Agilent) on a Bioanalyzer 2100 and the Qubit High Sensitivity DNA Assay (Thermo Fisher Scientific). The libraries were sequenced on NovaSeq6000 (Illumina) using 2 × 150 chemistry.

Single-cell RNA-sequencing (scRNA-seq) data processing reads were processed using the Cell Ranger 3.0.1 pipeline with default and recommended parameters. FASTQs generated from Illumina sequencing output were aligned to the mouse genome, version mm10, using the STAR algorithm. Next, Gene-Barcode matrices were generated for each individual sample by counting UMIs and filtering non-cell associated barcodes.

scRNA-sequencing data processing

R package Seurat was used for cell filtration, normalization, principal component analysis, variable genes finding, clustering analysis, and Uniform Manifold Approximation and Projection (UMAP) dimensional reduction. All functions were run with default parameters, unless specified otherwise. Low quality cells (<200 genes/cell or >2500 genes/cell, <3 cells/ gene, and >5% mitochondrial genes) were excluded.

Identification of cell clusters

The Seurat package implemented in R was applied to identify major cell types. Highly variable genes were generated and used to perform PCA. Significant principal components were determined using JackStraw analysis and visualization of heatmaps focusing on PCs 1 to 20. PCs 1 to 15 were used for graph-based clustering at res = 0.5 to identify distinct groups of cells. These groups were projected onto UMAP analysis run using previously computed principal components 1 to 20. The Seurat functions Vlnplot, FeaturePlot, DotPlot, and DoHeatmap were used to visualize the gene expression with violin plot, feature plot, dot plot, and heatmap, respectively.

Identification of cluster markers

We used the "FindAllMarkers" function in Seurat to identify genes that are differentially expressed between clusters with the following parameters: min.pct = 0.25, logfc.threshold = 0.25, only.pos = T. The non-parametric Wilcoxon rank-sum test was used to obtain p-values for comparisons, and the adjusted *p*-values, based on Bonferroni correction, for all genes in the dataset. We used heatmap to visualize DEGs based on gene expression after the log-transformed and scaling.

Cell-cell communication analysis

Using CellChat and CellphoneDB, cell-cell communication was inferred with the single-cell transcriptomic dataset. Briefly, according to the expression of a ligand by one lineage and a receptor by another, potential ligand-receptor interactions were predicted. For each ligand–receptor pair, we obtained a *P* value for the likelihood of lineage-specificity.

Bulk RNA-sequencing analysis

Bulk transcriptome data were derived from the publicly accessible dataset GSE52093 from GEO database, which contained 12 samples, including 7 from dissected aortic tissue and 5 from healthy aortic tissue.

Proteomic analysis

Proteomic data was obtained from plasma samples of 30 patients with AD and 30 matched healthy individuals based on a 4D data-independent acquisition (DIA) mass spectrometry platform. To reduce the confounding bias of unintended variables, propensity score matching was conducted with the following parameters: nearest-neighbor matching (1:1) with a calliper of 0.2; exact matching for age at onset and gender. Matching quality was evaluated by comparing baseline characteristics between patients with AD and matched healthy subjects. Serum samples were prepared for LC-MS/MS analysis as previously published[61]. In brief, serum proteins were denatured, alkylated, digested, and peptides purified using an automated liquid handling platform in a 96 well format. Separation was performed using the nanoflow Evosep One system (Evosep, Denmark), coupled to a timsTOF Pro mass spectrometer (Bruker, Bremen, Germany) equipped with a CaptiveSpray ion source. A 4D-DIA approach was applied on a Bruker timsTOF Pro instrument, operated in the PASEF mode with 10 PASEF scans per acquisition cycle and accumulation and ramp times of 100 ms each. Ionization was conducted in positive ion mode with a mass range of 100–1700 m/z. The 1/K0 ion mobility range was set to 0.6–1.6 V s/cm^2. The raw 4D-DIA data were processed using MaxQuant (version 1.5.2.8). The difference of protein expression patterns was quantitatively analyzed using edegR in R. The threshold of p values was determined by controlling false discovery rate (FDR). The corrected *p* value (*p*.adjust value) was *q* value. A fold change (FC), calculated based on the FPKM value, was defined as a differentially expressed gene (DEG) with a value of *q* (or *p*.adjust) <0.05 after the comparison of 2 data. The absolute value of Log2 expression ratio is greater than 1. Genomes The Gene Ontology (GO) and Kyoto Encyclopaedia of Genes and Genomes (KEGG) analysis results are displayed as bubble graphs.

Integrated scRNA and bulk RNA-sequencing analysis

The integrated analysis was performed using the Scissor algorithm[62], which can identify cell subsets that drive phenotypes (such as disease progression, tumor metastasis, immunotherapy response, and survival outcomes) in scRNA-seq data based on phenotypic information from bulk RNA sequencing (bulk-seq) data, also the cell subsets that are highly related to disease, thus revealing the possible molecular mechanisms. The Scissor algorithm firstly eliminates batch effect of bulk-seq and scRNA-seq, and establish the similarity network between cells based on scRNA-seq. The Pearson correlation coefficient between the scRNA-seq and bulk-seq expression data was denoted as S. The correlation matrix S was used as the decision variable and phenotypic data as the response variable to establish the regression relationship. The regression coefficient was set as β. The cells with positive and negative or non-zero regression coefficient β were represented as Scissor^{+} cells and Scissor^{-} cells, respectively. The alpha value of 0.05 was adopted in the regression model. The Scissor-captured cells was shown in feature plots. Functional enrichment analysis was performed on Scissor-positive cells, and the results were shown in bar charts.

Prognostic cohort design

This study complies in full with the STROBE statement. We prospectively collected and analyzed the clinical data of patients with type B aortic dissection who underwent endovascular therapy in the Zhongshan Hospital of Fudan University between November 2016 and November 2020. Patients were included if they were diagnosed with complicated type B AD, which was confirmed through computed tomography angiography (CTA) and had signed informed consent for TEVAR. Patient demographics and baseline information were recorded by medical record. The blood samples were collected before TEVAR.

Measurement of human plasma

Peripheral, human venous blood was drawn into prechilled citrate, theophylline, adenosine, dipyridamole-containing tubes for processing within 60 minutes of collection. The plasma was obtained by centrifugation of whole blood at 8000 × *g* at 4 °C for 20 minutes and stored in aliquots at −80 °C. The plasma samples were diluted 1:2, and CitH3 levels were measured using the Citrullinated Histone H3 ELISA Kit, following the manufacturer's instructions (501620, Cayman Chemical). The NET markers MPO, NE, IL-1β, IL-6 were measured by ELISA kit (Thermo Fisher). Circulating cell-free DNA was quantified in NET samples by using Quant-iT™ PicoGreen® dsDNA (P7589, Invitrogen).

Mice and in vivo experimental strategies

All animal experiments were approved by the Institutional Animal Care and Use Committee at Zhongshan Hospital. Wild-type C57BL/6 J male 3-week-old mice were used in this study and were purchased from the Beijing Vital River Laboratory Animal Technology. The mice were housed in the animal facility of Zhongshan Hospital, maintained under a 12-hour light/dark cycle, at a controlled ambient temperature of 22 ± 2 °C with a humidity level of 50 ± 10%. They had unrestricted access to food and water throughout the study. Unchallenged 3-week-old male control mice were fed a chow diet and infused with saline. Mice were randomly assigned to experimental groups using a computer-generated random number sequence to ensure unbiased allocation. The challenged three-week-old male WT mice were challenged with β-aminopropionitrile (BAPN) for 4 weeks. BAPN was administered in drinking water with the dose at 5 mg/mL (0.5% wt/vol). Four weeks later, the mice were infused with Ang II (1000 ng/kg/min) with mini-osmotic pumps (Model 1003D, Alzet) for 3 days to induce AD.

During the four-week of BAPN infusion period, the challenged mice were also given daily intraperitoneal injections of either PBS ($n = 12$), or Cl-amidine (10 mg/kg, Sigma-Aldrich) ($n = 12$), or DNase I (5 mg/kg, Roche Diagnostics) ($n = 12$) or the combination of Cl-amidine and DNase I ($n = 12$) for 3 weeks from the 4 weeks of age.

In the second experiment, the challenged mice were treated with either isotype control antibody ($n = 12$) or CXCL3 antibody (2 mg/kg, AF5568, R&D systems, Minneapolis, MN, USA) ($n = 12$) or CXCR2 antibody (2 mg/kg, MAB2164-100, R&D systems, Minneapolis, MN, USA) ($n = 12$) intraperitoneally, every three days, starting at 1 week after BAPN administration.

Baseline aortic diameter of each mouse was measured by ultrasound. The dead mice were immediately dissected and the surviving mice were euthanized at the end of the 4-week study period. The aortas were exposed and rinsed with cold PBS, and the periaortic tissues were removed. The aorta was then excised, further cleaned, and rinsed with cold PBS to remove any residual blood in the lumen. Next, aortas were imaged for diameter measurement and disease evaluation. Each mouse aorta was stained for H&E to observe AD occurrence, characterized by elastin degradation and rupture in aortic media layer. Aortic wall thickness and media thickness were measured through the images determined by H&E, elastic, and collagen fiber staining. Maximum and minimum values of the wall thickness and media thickness were measured in each image and calculated the averages. To reduce bias, experiments were conducted in a blinded manner. Researchers responsible for data collection and analysis were unaware of the group allocations during the study.

Hematoxylin and eosin staining and elastic and collagen fiber staining

Aortic sections were stained with hematoxylin and eosin, Masson's trichrome and Verhoeff–van Gieson elastin stain, according to the manufacturer's instructions. Aortic sections were examined by 2 independent observers who were blinded to the experimental groups to confirm the occurrence of AD rather than the possible incidence of aneurysm. Elastin degradation was graded according to following criteria: I: 0–25%; II: 26–50%; III: 51–75%; IV: 76–100%.

Multiplex immunohistochemical of tissue sections

Tyramide signal amplification was applied to enhance the fluorescence amplification signal and to avoid limit to the species origin of primary antibody[63,64]. All aortic tissue samples were formalin fixed, paraffin embedded, and 5 μm sections were subjected to antigen retrieval in citrate buffer, then permeabilized and stained. Human aortic tissue samples were then permeabilized and stained with rabbit MPO antibody (ab208670, Abcam, Ltd., Cambridge, UK) at 1 mg/mL, polyclonal rabbit CitH3 antibody (ab5103, Abcam, Ltd., Cambridge, UK) at 1 mg/mL, rabbit CXCL3 antibody (AV07037, Sigma-Aldrich Co., St. Louis, MO, USA) at 1 mg/mL, and with rabbit CXCR2 antibody (ab225732, Abcam, Ltd., Cambridge, UK) at 1 mg/mL. Mouse aortic tissue samples were then permeabilized and stained with rabbit Ly6G antibody (ab238132, Abcam, Ltd., Cambridge, UK) at 2 mg/mL, rabbit CitH3 antibody (ab5103, Abcam, Ltd., Cambridge, UK) at 1 mg/mL, rabbit CXCL3 antibody (ab220431, Abcam, Ltd., Cambridge, UK) at 1 mg/mL, and with rabbit CXCR2 antibody (bs-12257R, Bioss Inc. Woburn, Massachusetts, USA) at 1 mg/mL. Alexa Fluor 647 goat anti-mouse IgG and Alexa Fluor 555 donkey anti-rabbit IgG were applied at 1:1000 as secondary reagents; DNA was stained with DAPI at 1:1000 working dilution (all Thermo Fisher Scientific). Consecutive tissue sections were subjected to staining with hematoxylin and eosin for comparison.

Statistics and reproducibility

Continuous variables are presented as means with standard deviations (SDs) or as medians with interquartile ranges (IQRs). Non-parametric tests were used for group comparisons (Mann-Whitney U or Wilcoxon signed-rank test) or correlations (Spearman). Receiver operating characteristics (ROC) and time-dependent ROC analysis were served to evaluate the diagnostic and prognostic marker potential, respectively, by the area under the ROC curve (AUC). Least Absolute Shrinkage and Selection Operator (LASSO) and multivariable logistic regression analysis (Statistically significant variables on univariable Cox analysis) were conducted to assess the prognostic value of NETs associated markers for AAEs and identify independent risk factors. Multiple imputation was used to account for the missing data. A two-sided significance level of 0.05 was applied. Data analysis and visualization were performed with R software 4.2 (R Foundation for Statistical Computing, Vienna, Austria) and GraphPad Prism 8.0 (GraphPad Software, San Diego, CA, USA).

Reporting summary

Further information on research design is available in the Nature Portfolio Reporting Summary linked to this article.

Data availability

The data supporting the findings from this study are available within the manuscript and its supplementary information. The raw data of single-cell RNA transcriptome data has been deposited in the GEO database under accession code GSE254132. The previously published bulk RNA transcriptome data has been deposited in the GEO database under

accession code GSE52093. The Proteome data used in this study are available from MassIVE under accession code MSV000093736. Source data are provided with this paper.

Code availability

The custom code has been deposited at GitHub and is available at https://github.com/Zhao-yufeiii/Aortic-Dissection.

References

1. Erbel, R. et al. 2014 ESC Guidelines on the diagnosis and treatment of aortic diseases: Document covering acute and chronic aortic diseases of the thoracic and abdominal aorta of the adult. The Task Force for the Diagnosis and Treatment of Aortic Diseases of the European Society of Cardiology (ESC). *Eur. Heart J.* **35**, 2873–2926 (2014).
2. Rylski, B., Schilling, O. & Czerny, M. Acute aortic dissection: evidence, uncertainties, and future therapies. *Eur. Heart J.* **44**, 813–821 (2023).
3. Afifi, R. O. et al. Outcomes of patients with acute type B (DeBakey III) Aortic dissection: a 13-year, single-center experience. *Circulation* **132**, 748–754 (2015).
4. Garbade, J. et al. Outcome of patients suffering from acute type B aortic dissection: a retrospective single-centre analysis of 135 consecutive patients. *Eur. J. Cardiothorac. Surg.* **38**, 285–292 (2010).
5. Ogami, T. et al. Long-term outcomes after recurrent acute thoracic aortic dissection: Insights from the International Registry of Aortic Dissection. *J. Thorac. Cardiovasc. Surg.* **24**, 283–286 (2024).
6. Payne, D. et al. Five-year outcomes of endovascular treatment for aortic dissection from the Global Registry for Endovascular Aortic Treatment. *J. Vasc. Surg.* **24**, 1234–1235 (2024).
7. Kato, M. et al. Determining surgical indications for acute type B dissection based on enlargement of aortic diameter during the chronic phase. *Circulation* **92**, Ii107–Ii112 (1995).
8. Song, J. M. et al. Long-term predictors of descending aorta aneurysmal change in patients with aortic dissection. *J. Am. Coll. Cardiol.* **50**, 799–804 (2007).
9. Marui, A., Mochizuki, T., Koyama, T. & Mitsui, N. Degree of fusiform dilatation of the proximal descending aorta in type B acute aortic dissection can predict late aortic events. *J. Thorac. Cardiovasc Surg.* **134**, 1163–1170 (2007).
10. Evangelista, A. et al. Long-term outcome of aortic dissection with patent false lumen: predictive role of entry tear size and location. *Circulation* **125**, 3133–3141 (2012).
11. Kitai, T. et al. Impact of new development of ulcer-like projection on clinical outcomes in patients with type B aortic dissection with closed and thrombosed false lumen. *Circulation* **122**, S74–S80 (2010).
12. Marui, A. et al. Toward the best treatment for uncomplicated patients with type B acute aortic dissection: a consideration for sound surgical indication. *Circulation* **100**, Ii275–Ii280 (1999).
13. Tsai, T. T. et al. Partial thrombosis of the false lumen in patients with acute type B aortic dissection. *N. Engl. J. Med.* **357**, 349–359 (2007).
14. Li, D. et al. Predictor of false lumen thrombosis after thoracic endovascular aortic repair for type B dissection. *J. Thorac. Cardiovasc Surg.* **160**, 360–367 (2020).
15. Suzuki, T. et al. Diagnosis of acute aortic dissection by D-dimer: the International Registry of Acute Aortic Dissection Substudy on Biomarkers (IRAD-Bio) experience. *Circulation* **119**, 2702–2707 (2009).
16. Zhao, Y., Fu, W. & Wang, L. Biomarkers in aortic dissection: Diagnostic and prognostic value from clinical research. *Chin. Med J. (Engl.)* **137**, 257–269 (2024).
17. Ainiwan, M., Wang, Q., Yesitayi, G. & Ma, X. Identification of FERMT1 and SGCD as key marker in acute aortic dissection from the perspective of predictive, preventive, and personalized medicine. *EPMA J.* **13**, 597–614 (2022).
18. Yofe, I., Dahan, R. & Amit, I. Single-cell genomic approaches for developing the next generation of immunotherapies. *Nat. Med.* **26**, 171–177 (2020).
19. Wu, Y. et al. Neutrophil profiling illuminates anti-tumor antigen-presenting potency. *Cell* **187**, 1422–1439.e1424 (2024).
20. Sattler, S. Single-cell immunology in cardiovascular medicine: do we know yet what we do not know? *Circulation* **144**, 843–844 (2021).
21. Sun, D. et al. Identifying phenotype-associated subpopulations by integrating bulk and single-cell sequencing data. *Nat. Biotechnol.* **40**, 527–538 (2022).
22. Weinstein, J. N. et al. The Cancer Genome Atlas Pan-Cancer analysis project. *Nat. Genet.* **45**, 1113–1120 (2013).
23. Otsuka, K. et al. Suppression of inflammation in rat autoimmune myocarditis by S100A8/A9 through modulation of the proinflammatory cytokine network. *Eur. J. Heart Fail.* **11**, 229–237 (2009).
24. Laouedj, M. et al. S100A9 induces differentiation of acute myeloid leukemia cells through TLR4. *Blood* **129**, 1980–1990 (2017).
25. Condamine, T. et al. Lectin-type oxidized LDL receptor-1 distinguishes population of human polymorphonuclear myeloid-derived suppressor cells in cancer patients. *Sci. Immunol.* **1**, aaf8943 (2016).
26. Cochain, C. et al. Single-cell RNA-seq reveals the transcriptional landscape and heterogeneity of aortic macrophages in murine atherosclerosis. *Circulation Res.* **122**, 1661–1674 (2018).
27. Ensan, S. et al. Self-renewing resident arterial macrophages arise from embryonic CX3CR1(+) precursors and circulating monocytes immediately after birth. *Nat. Immunol.* **17**, 159–168 (2016).
28. Beckers, C. M. L. et al. Cre/lox studies identify resident macrophages as the major source of circulating coagulation factor XIII-A. *Arterioscler Thromb. Vasc. Biol.* **37**, 1494 (2017). +.
29. Puellmann, K. et al. A variable immunoreceptor in a subpopulation of human neutrophils. *Proc. Natl Acad. Sci. USA* **103**, 14441–14446 (2006).
30. Fuchs, T. et al. The macrophage-TCR alpha beta is a cholesterol-responsive combinatorial immune receptor and implicated in atherosclerosis. *Biochem. Biophys. Res. Commun.* **456**, 59–65 (2015).
31. Beham, A. W. et al. A TNF-regulated recombinatorial macrophage immune receptor implicated in granuloma formation in tuberculosis. *PLoS Pathog.* **7**, e1002375 (2011).
32. Zhang, Y. et al. A signature for pan-cancer prognosis based on neutrophil extracellular traps. *J. Immunother. Cancer* **10** (2022).
33. Lewis, H. D. et al. Inhibition of PAD4 activity is sufficient to disrupt mouse and human NET formation. *Nat. Chem. Biol.* **11**, 189–191 (2015).
34. Ahuja, S. K. & Murphy, P. M. The CXC chemokines growth-regulated oncogene (GRO) alpha, GRObeta, GROgamma, neutrophil-activating peptide-2, and epithelial cell-derived neutrophil-activating peptide-78 are potent agonists for the type B, but not the type A, human interleukin-8 receptor. *J. Biol. Chem.* **271**, 20545–20550 (1996).
35. Zernecke, A. et al. Meta-analysis of leukocyte diversity in atherosclerotic mouse aortas. *Circ. Res.* **17**, 402–426 (2020).
36. Veglia, F., Sanseviero, E. & Gabrilovich, D. I. Myeloid-derived suppressor cells in the era of increasing myeloid cell diversity. *Nat. Rev. Immunol.* **21**, 485–498 (2021).
37. Sprenkeler, E. G. G., Zandstra, J. & van Kleef, N. D. S100A8/A9 is a marker for the release of neutrophil extracellular traps and induces neutrophil activation. *Cells* **11**, 236 (2022).

38. Lu, L. et al. C1q/TNF-related protein-1: an adipokine marking and promoting atherosclerosis. *Eur. Heart J.* **37**, 1762–1771 (2016).
39. Spivia, W., Magno, P. S., Le, P. & Fraser, D. A. Complement protein C1q promotes macrophage anti-inflammatory M2-like polarization during the clearance of atherogenic lipoproteins. *Inflamm. Res.* **63**, 885–893 (2014).
40. Son, M. et al. C1q and HMGB1 reciprocally regulate human macrophage polarization. *Blood* **128**, 2218–2228 (2016).
41. Schott, J. et al. Translational regulation of specific mRNAs controls feedback inhibition and survival during macrophage activation. *PLoS Genet.* **10**, e1004368 (2014).
42. Pothineni, N. V. K. et al. LOX-1 in atherosclerosis and myocardial ischemia biology, genetics, and modulation. *J. Am. Coll. Cardiol.* **69**, 2759–2768 (2017).
43. Majesky, M. W. Developmental basis of vascular smooth muscle diversity. *Arterioscler Thromb. Vasc. Biol.* **27**, 1248–1258 (2007).
44. Li, Y. et al. Single-cell transcriptome analysis reveals dynamic cell populations and differential gene expression patterns in control and aneurysmal human aortic tissue. *Circulation* **142**, 1374–1388 (2020).
45. Liu, X. et al. Single-cell RNA sequencing identifies an Il1rn(+)/Trem1(+) macrophage subpopulation as a cellular target for mitigating the progression of thoracic aortic aneurysm and dissection. *Cell Discov.* **8**, 11 (2022).
46. Emoto, T. et al. Single-cell RNA sequencing reveals a distinct immune landscape of myeloid cells in coronary culprit plaques causing acute coronary syndrome. *Circulation* **145**, 1434–1436 (2022).
47. Swirski, F. K. & Nahrendorf, M. Leukocyte behavior in atherosclerosis, myocardial infarction, and heart failure. *Science* **339**, 161–166 (2013).
48. Doring, Y., Drechsler, M., Soehnlein, O. & Weber, C. Neutrophils in atherosclerosis from mice to man. *Arterioscler Thromb. Vasc. Biol.* **35**, 288–295 (2015).
49. Horckmans, M. et al. Neutrophils orchestrate post-myocardial infarction healing by polarizing macrophages towards a reparative phenotype. *Eur. Heart J.* **38**, 187–197 (2017).
50. Gessler, N. et al. Sleep apnea predicts cardiovascular death in patients with Marfan syndrome: a cohort study. *EPMA J.* **13**, 451–460 (2022).
51. Zhan, X., Li, J., Guo, Y. & Golubnitschaja, O. Mass spectrometry analysis of human tear fluid biomarkers specific for ocular and systemic diseases in the context of 3P medicine. *EPMA J.* **12**, 449–475 (2021).
52. Golubnitschaja, O. et al. Ischemic stroke of unclear aetiology: a case-by-case analysis and call for a multi-professional predictive, preventive and personalised approach. *EPMA J.* **13**, 535–545 (2022).
53. Silvestre-Roig, C., Braster, Q., Ortega-Gomez, A. & Soehnlein, O. Neutrophils as regulators of cardiovascular inflammation. *Nat. Rev. Cardiol.* **17**, 327–340 (2020).
54. Papayannopoulos, V. & Zychlinsky, A. NETs: a new strategy for using old weapons. *Trends Immunol.* **30**, 513–521 (2009).
55. Warnatsch, A., Ioannou, M., Wang, Q. & Papayannopoulos, V. Inflammation. Neutrophil extracellular traps license macrophages for cytokine production in atherosclerosis. *Science* **349**, 316–320 (2015).
56. Dhawan, U. K., Bhattacharya, P., Narayanan, S., Manickam, V. & Aggarwal, A. Hypercholesterolemia impairs clearance of neutrophil extracellular traps and promotes inflammation and atherosclerotic plaque progression. *Arterioscler Thromb. Vasc. Biol.* **41**, 2598–2615 (2021).
57. Meher, A. K. et al. Novel role of IL (Interleukin)-1β in neutrophil extracellular trap formation and abdominal aortic aneurysms. *Arterioscler Thromb. Vasc. Biol.* **38**, 843–853 (2018).
58. Daniel, C. et al. Extracellular DNA traps in inflammation, injury and healing. *Nat. Rev. Nephrol.* **15**, 559–575 (2019).
59. Borissoff, J. I. et al. Elevated levels of circulating DNA and chromatin are independently associated with severe coronary atherosclerosis and a prothrombotic state. *Arterioscler Thromb. Vasc. Biol.* **33**, 2032–2040 (2013).
60. Eilenberg, W. et al. Histone citrullination as a novel biomarker and target to inhibit progression of abdominal aortic aneurysms. *Transl. Res.* **233**, 32–46 (2021).
61. Geyer, P. E. et al. Plasma proteome profiling to assess human health and disease. *Cell Syst.* **2**, 185–195 (2016).
62. Sun, D., Guan, X. & Moran, A. E. Identifying phenotype-associated subpopulations by integrating bulk and single-cell sequencing data. *Nat. Biotechnol.* **40**, 527–538 (2022).
63. Bobrow, M. N., Harris, T. D., Shaughnessy, K. J. & Litt, G. J. Catalyzed reporter deposition, a novel method of signal amplification. Application to immunoassays. *J. Immunol. Methods* **125**, 279–285 (1989).
64. Zhang, L. et al. Lineage tracking reveals dynamic relationships of T cells in colorectal cancer. *Nature* **564**, 268–272 (2018).

Acknowledgements

This study was supported by the National Science Foundation of China (no. 82270415; to Wang LX), Shanghai Municipal Health Commission's Health Industry Research Project (no. 20234Z0012; to Wang LX), Shanghai Municipal Science and Technology Commission Innovation Fund (no. 22S31904800; to Wang LX), Fujian Province Health Science and Technology Fund (no. 2021GGB030; to Hong SC), Fudan Zhangjiang Clinical Medicine Innovation Fund (no. KP7202115; to Wang LX), Shanghai Oriental Talent Program Top Project (no. SSF828071; to Wang LX). We thank Prof. Dan Meng (Fudan University), Prof. Chenji Wang (Fudan University), Dr. Jianming Zeng (University of Macau) for their support in this work. This work was supported by the Medical Science Data Center in Shanghai Medical College of Fudan University.

Author contributions

Conceptualization: Y.-F.Z., L.-X.W. Methodology: Y.-F.Z., Z.-A.Z, Z.-Y.L., Y.Y., S.-C.H. Investigation: Y.-F.Z. Visualization: Y.-F.Z., Z.-A.Z. Funding acquisition: L.-X.W., W.-G.F. Project administration: L.-X.W. Supervision: L.-X.W., B.Z. Writing—original draft: Y. Writing—review & editing: L.-X.W.

Competing interests

The authors declare no competing interests.

Additional information

Supplementary information The online version contains supplementary material available at https://doi.org/10.1038/s41467-024-55038-8.

Correspondence and requests for materials should be addressed to Li-Xin Wang.

Peer review information *Nature Communications* thanks Olga Golubnitschaja, Wei Guo, and the other, anonymous, reviewer for their contribution to the peer review of this work. A peer review file is available.